INTERFACE

rsif.royalsocietypublishing.org

Research

Cite this article: Marino M, Pontrelli G, Vairo G, Wriggers P. 2017 A chemo-mechano-biological formulation for the effects of biochemical alterations on arterial mechanics: the role of molecular transport and multiscale tissue remodelling. *J. R. Soc. Interface* **14**: 20170615.
http://dx.doi.org/10.1098/rsif.2017.0615

Received: 23 August 2017
Accepted: 11 October 2017

Subject Category:
Life Sciences–Engineering interface

Subject Areas:
biomechanics, biomedical engineering, biomathematics

Keywords:
arterial multiphysics, multiscale constitutive modelling, microscale transport mechanisms, tissue remodelling, vascular pathologies

Author for correspondence:
Michele Marino
e-mail: marino@ikm.uni-hannover.de

THE ROYAL SOCIETY PUBLISHING

A chemo-mechano-biological formulation for the effects of biochemical alterations on arterial mechanics: the role of molecular transport and multiscale tissue remodelling

Michele Marino[1], Giuseppe Pontrelli[2], Giuseppe Vairo[3] and Peter Wriggers[1]

[1]Institut für Kontinuumsmechanik, Leibniz Universität Hannover, Hannover, Germany
[2]Istituto per le Applicazioni del Calcolo, National Research Council (CNR), Rome, Italy
[3]Dipartimento di Ingegneria Civile e Ingegneria Informatica, Università degli Studi di Roma 'Tor Vergata', Rome, Italy

MM, 0000-0002-4323-3061; GP, 0000-0003-0659-210X; GV, 0000-0003-2597-6985; PW, 0000-0002-2676-1145

This paper presents a chemo-mechano-biological framework for arterial physiopathology. The model accounts for the fine remodelling in the multi-scale hierarchical arrangement of tissue constituents and for the diffusion of molecular species involved in cell–cell signalling pathways. Effects in terms of alterations in arterial compliance are obtained. A simple instructive example is introduced. Although oversimplified with respect to realistic case studies, the proposed application mimics the biochemical activity of matrix metallo-proteinases, transforming growth factors beta and interleukins on tissue remodelling. Effects of macrophage infiltration, of intimal thickening and of a healing phase are investigated, highlighting the corresponding influence on arterial compliance. The obtained results show that the present approach is able to capture changes in arterial mechanics as a consequence of the alterations in tissue biochemical environment and cellular activity, as well as to incorporate the protective role of both autoimmune responses and pharmacological treatments.

1. Introduction

The healthy physiological response of the cardiovascular system is related to the biomechanical performances of arterial structures [1]. Cardiovascular diseases highly affect the correct functioning of the human body, being the leading cause of deaths worldwide [2]. Although it is well known that pathologies are driven by the biological activity of cells in response to both biomechanical and biochemical stimuli [3], the etiology of a number of arterial pathologies is still debated [2]. This is due to the complexity of the biomechanical/biochemical environment of arterial tissues, and leads to the fact that therapeutic approaches are usually driven by the risk ranges deduced via clinical records [2].

Many biochemical substances (such as oxygen, nutrients, hormones, enzymes, proteins, growth factors and sometimes drugs) are dispersed in a living body, with concentrations controlled by complex regulatory mechanisms. These substances play a crucial role in inflammatory states, mechanical dysfunctions and degradation of constituents of the extracellular matrix (ECM) [3–5].

The ECM provides the necessary physical scaffolding and serves as a source of crucial biochemical and biomechanical signals which, in turn, regulate tissue morphogenesis, differentiation and homeostasis [4,6,7]. ECM remodels through a change in tissue structure, achieved by the reorganization of existing constituents or by the synthesis of new constituents. Remodelling may or not alter the mass density, but it does change tissue stiffness and strength properties which are mainly conferred by the elastin network and collagen fibres.

The dysregulation of ECM degradation and deposition leads to pathological remodelling of cardiovascular tissues which remain an open issue still under investigation [4,8–14]. In turn, ECM structure has a major influence on tissue mechanical properties and is affected by the biochemical activity of soluble molecules. For instance, the synthesis/degradation of ECM constituents is regulated by cell–cell signalling pathways involving matrix metalloproteinases (MMPs), transforming growth factors-β (TGFs-β), interleukins (ILs) and many other molecules [4,8–17].

As a consequence, molecular transport phenomena highly affect the macroscale mechanics of organs and macrobiological structures. Moreover, as cells respond to mechanical stimuli by altering the biochemical environment, mechanical quantities also affect transport phenomena in a closed feedback loop [7,15].

As illustrative examples, an increased production of ILs by macrophages and of MMPs by smooth muscle cells (SMCs) characterize inflammatory states which play an important role during the development of aneurysms [10,18]. Furthermore, the coupling of these inflammatory states with pathological conditions that alter molecular diffusion mechanisms (e.g. reduced permeability due to intimal atherosclerotic or hyperplastic thickening) enhances arterial dilation [18,19]. On the other hand, autoimmune or pharmacological mechanisms increasing the production of TGF-β play a protective role versus aneurysm formation [20].

Under this perspective, the analysis of physiopathological mechanisms in arterial structures should be addressed via a multiphysics strategy taking into account the interaction between transport processes and mechanics. This would surely lead to a better understanding of the onset of many pathologies and to the development of novel therapeutic and clinical approaches.

Accordingly, starting from the strategy traced by authors in [21] and in the framework of continuum mechanics, a novel chemo-mechano-biological formulation addressing arterial physiopathology is employed in the present paper. The proposed approach faces two common limitations of available models for describing arterial growth and remodelling in disease [22–31].

First of all, in the existing literature, molecular transport mechanisms involved in cell–cell signalling pathways are generally not accounted for in growth–remodelling approaches. An insight into the biophysical factors that influence the molecular transport can be gained by modelling and computational approaches for the solution of reaction–diffusion equations, as already applied in contexts not associated with growth–remodelling [32–37].

Moreover, available growth–remodelling models are based on a description of tissue nonlinear mechanics via strain-energy functions that disregard any direct relationship with micro- and nanoscale mechanisms. The nonlinearities of constituents are indeed generally taken into account by choosing a suitable analytical form of the strain-energy density (e.g. polynomial, exponential) as in a phenomenological approach [38–41]. Therefore, existing growth and remodelling approaches are generally able to account only for coarse changes on tissue composition or, at most, for the realignment of collagen fibres [22–31]. As a consequence, these models cannot analyse the macroscopic effects of fine alterations in tissue histological and biochemical features, instrumental in cardiovascular pathologies [13,42–46]. As a matter of fact, as stated by Cyron *et al.* [23], it is generally assumed that *mass turnover does not change the general mechanical behaviour of a constituent (i.e. its strain energy function), only its average stress-free configuration*. By contrast, multiscale homogenization techniques have been recently proposed by some authors in order to derive tissue mechanics as a function of nano- and microscale mechanisms and, hence, introducing fine histological, biochemical and biophysical properties as model parameters [47–53].

This paper presents a first application of the general multiphysics modelling strategies traced by the authors in [21] for the description of the alterations of arterial mechanics due to physiopathological mechanisms. The aim is to show the capability of the employed formulation in shedding a light on the role of (i) imbalances of cell–cell signalling pathways, modelled by accounting for the transport of molecular species within tissues, and (ii) alterations in the general mechanical behaviour of constituents (i.e. tissue strain energy), incorporated by means of the multiscale constitutive description developed by some of the authors [47–53]. In particular, constitutive alterations are accounted for by instructing the model with fine changes in histological/biochemical properties during ECM remodelling, and discriminating these effects from possible mass/density changes. Therefore, the perspective of this paper is complementary to the one in the mainstream of growth and remodelling approaches [22–31].

An instructive example is introduced (see §2), with geometry and simulation conditions considered as simple as possible, in order to focus on the role of the mechanisms of interest. Remarkably, an analytical solution could be obtained. The proposed case study addresses some crucial chemo-biological phenomena involved in the evolution of arterial pathological dilation: the onset of an inflammatory state (e.g. associated with the infiltration of macrophages); alterations in the washout of molecules in the arterial lumen (e.g. induced by the presence of atherosclerotic plaques); an increased production of growth factors (e.g. induced by a pharmacological treatment). ECM remodelling is driven by intra-arterial-wall transport of MMPs, TGFs-β and ILs. Fine alterations in tissue microstructure (e.g. in thickness of collagen fibres) and in biochemical properties (e.g. in the density of intermolecular cross-links) are accounted for, together with variations in collagen/elastin volume fractions and in the dispersed arrangement of collagen fibres. Effects on the compliance of an artery-like cylindrical structure are analysed.

Although the application is highly simplified and not representative of realistic scenarios, presented results (see §3) show the potentialities offered by the present multiphysics chemo-mechano-biological formulation (see §4). Technical details of the proposed model and the corresponding governing equations are reported in §5 (Material and methods).

2. Arterial multiphysics behaviour

Arteries are cylinder-like structures, usually composed of three layers: the tunica intima, tunica media and tunica adventitia (from inner to outer) [54–57]. From a mechanical viewpoint, the main constituents of arterial tissues are collagen and elastin (figure 1). While elastin forms a quasi-isotropic network, collagen is found in the form of fibres. The latter are characterized

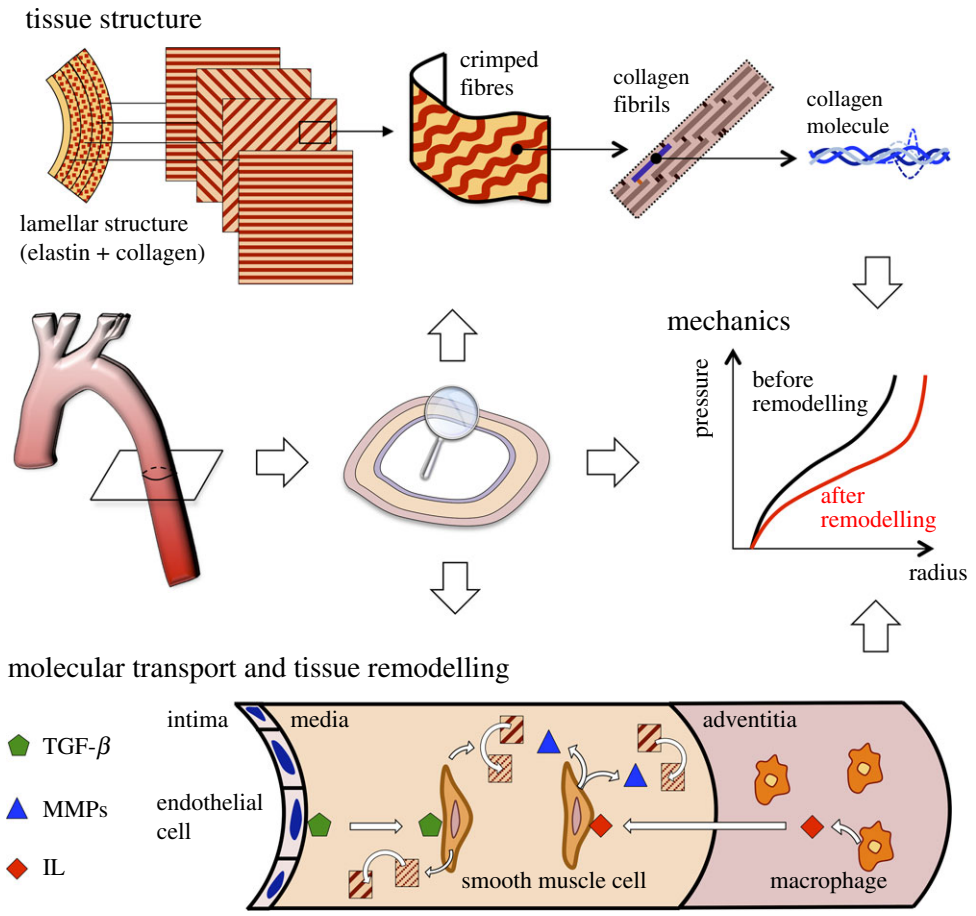

Figure 1. Arterial multiphysics: coupling of molecular transport phenomena, multiscale mechanics and physiopathological remodelling of tissue constituents. TGF-β, transforming growth factor beta; MMPs, matrix metalloproteinases; IL, interleukin.

by a crimped microstructure and are helically wrapped around the vessel axis. In both media and adventitia, collagen fibres are mainly aligned along a well-defined orientation, although a non-negligible angular dispersion has been widely reported [54,55]. In particular, the main direction of collagen fibres is close to the circumferential direction in the media and to the axial one in the adventitia, resulting in arterial compliance mainly affected by the mechanics of the tunica media.

As schematically depicted in figure 1, the pressure–radius relationship of an arterial segment is characterized by a relatively high distensibility at low pressures (mainly associated with the elastin content) and a stiffening response for high pressures (related to the progressive stiffening induced by the straightening of crimped collagen fibres) [56,58]. Accordingly, the arrangement and composition of ECM has a strong influence on the macroscopic functional behaviour of arterial segments. In turn, ECM remodels due to cell–cell signalling pathways [4,8,9,12–14] which involve transport mechanisms [59]. Although most of these pathways are still not completely clarified, it is generally recognized that cells respond to alterations in biochemical and loading conditions via altered gene expression, and hence producing molecules that intervene in ECM remodelling [10,11,60,61]. Under homeostatic conditions, the balance between ECM degradation and reinforcement is promoted by the equilibrium of cell–cell signalling pathways. A loss of the control of these activities may result in diseases.

2.1. Case study

The case study addresses cell–cell signalling pathways involving MMPs, TGFs-β and ILs and their effects on ECM remodelling mechanisms that determine arterial dilation towards the etiology of aneurysms. A schematic of the case study is provided in figure 2.

Two cell–cell signalling pathways are considered: macrophages in the adventitia produce ILs that, in turn, activate SMCs in the media to synthesize MMPs [60,61]; endothelial cells in the intima produce TGFs-β that inhibit the synthesis of MMPs by SMCs in the media [9–11]. Therefore, introducing c_1, c_2 and c_3 as the concentrations of MMPs, TGFs-β and ILs, respectively, the molecular transport problem T is defined in terms of the following relationships (figure 2):

$$\mathsf{T}:\begin{cases} c_1 \text{ decreases when } c_2 \text{ increases,} \\ c_1 \text{ increases when } c_3 \text{ increases,} \\ c_2 \text{ increases when the activity of endothelial cells increases,} \\ c_3 \text{ increases when the activity of macrophages increases.} \end{cases} \tag{2.1}$$

The solution of transport problem T gives the value of the vector $\mathbf{c} = (c_1, c_2, c_3)$ which describes the tissue biochemical environment at hand.

The ECM structural features subject to remodelling are as follows: the volume fraction V_E of elastin network; the volume fraction V_C of collagen fibres; the radius measure r_F of collagen fibres (i.e. half of the fibre thickness); the density Λ_c of inter-molecular cross-links between collagen molecules; and a measure μ_F of the standard deviation of the fibre orientation distribution. In detail, assuming a bimodal distribution for the latter, μ_F^{-1} is directly proportional to the number of fibres aligned along the two preferred directions. These

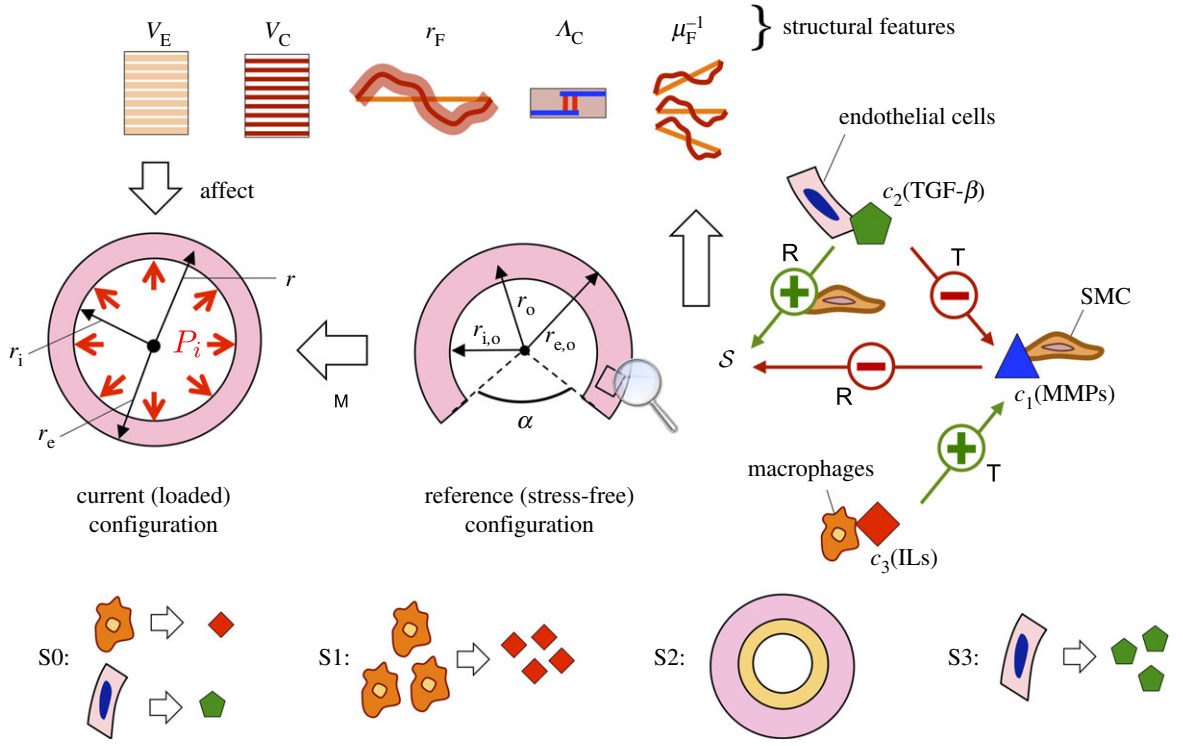

Figure 2. Schematic of the case study introduced in §2.1. Cell–cell signalling pathways governing molecular concentrations c_1, c_2 and c_3 by means of the transport problem T (see equation (2.1)). Remodelling laws R (see equation (2.3)) for structural features in set $\mathcal{S}$ (see equation (2.2)), that is elastin volume fraction V_E, collagen volume fraction V_C, radius r_F of collagen fibres, density Λ_c of intermolecular cross-links, and the inverse of standard deviation measure μ_F^{-1} of collagen fibres orientation distribution. Mechanical problem M for obtaining arterial current (loaded) configuration (P_i: luminal pressure; r_i (r_e): internal (external) radius; r: radial coordinate) from the (stress-free) reference configuration (α: opening angle; $r_{i,o}$ ($r_{e,o}$): internal (external) radius; r_o: radial coordinate). Stages S0, S1, S2 and S3 of the addressed physiopathological mechanism. TGF-β, transforming growth factor beta; MMPs, matrix metalloproteinases; IL, interleukin; SMC, smooth muscle cell. For model details, readers can refer to §5.

structural features will be denoted as s_j (with $j = 1 \dots 5$) and they are collected in set $\mathcal{S}$ defined as (figure 2)

$$\mathcal{S} = \{s_1 = V_E,\ s_2 = V_C,\ s_3 = r_F,\ s_4 = \Lambda_c,\ s_5 = \mu_F^{-1}\}. \quad (2.2)$$

To include the effects of molecular pathways on remodelling, a chemical-driven target value of histological/biochemical features s_j in $\mathcal{S}$ is introduced. In particular, the target value for s_j is $\bar{s}_j + \mathcal{I}_j(\mathbf{c})$. Here, $\bar{s}_j$ is a reference value corresponding to the homeostatic mechanical behaviour, and $\mathcal{I}_j(\mathbf{c})$ is the homeostatic imbalance. The latter depends on tissue biochemical environment $\mathbf{c}$, and thereby it is governed by cell–cell signalling pathways. Clearly, the healthy state occurs when the value of $\mathbf{c}$ is such that $\mathcal{I}_j(\mathbf{c}) = 0$, i.e. when cell–cell signalling pathways are balanced, resulting in $s_j = \bar{s}_j$. On the other hand, cell imbalances determine $\mathcal{I}_j(\mathbf{c}) \neq 0$, and thereby an evolution towards a non-healthy tissue structure characterized by $s_j \neq \bar{s}_j$.

In the specific case study herein addressed, remodelling laws for s_j are driven by the following biochemically motivated evidence: MMPs are proteinases that activate ECM degradation [4,14,16,17] and that determine the disorganization of ECM constituents [8,12]. On the other hand, TGFs-β activate SMCs to promote ECM deposition [10,11], to affect ECM cross-linking biochemistry [13] and to repress ECM degradation [9]. Accordingly, the value of s_j increases when the concentration c_2 of TGFs-β increases, and/or when the concentration c_1 of MMPs decreases. While MMPs degrade ECM constituents in a direct way, TGF-β activity is mediated by SMCs, characterized by the volume fraction V_S. In summary, as also depicted in figure 2, problem R for remodelling is formulated by defining the homeostatic imbalance $\mathcal{I}_j(\mathbf{c})$ such that (with $j = 1, \dots, 5$):

$$\mathsf{R}: \begin{cases} s_j \text{ decreases when } c_1 \text{ increases,} \\ s_j \text{ increases when } V_S c_2 \text{ increases.} \end{cases} \quad (2.3)$$

In particular, since physiopathological remodelling is herein addressed (i.e. reference is not made to a natural turnover process), remodelling is defined in the framework of a threshold-based approach: it is activated when c_1 and c_2, respectively, reach thresholds C_{R1} and C_{R2}. The solution of the remodelling problem gives the value of set $\mathcal{S}$ (see equation (2.2)) which describes tissue structure, and hence tissue mechanics, at hand.

Arterial compliance is obtained from the solution of the mechanical problem M, defined by considering an axisymmetric arterial segment and providing the relationship between the corresponding luminal pressure P_i and the internal radius r_i (figure 2). A multiscale approach is employed for describing the mechanics of arterial tissues, hence obtaining an explicit dependence on the values of structural features in set $\mathcal{S}$ (see equation (2.2)). As sketched in figure 2, arterial mechanics M is coupled with remodelling laws R in equation (2.3), in turn, affected by transport mechanisms T in equation (2.1).

The addressed pathological mechanism corresponds to biochemical alterations occurring over time $t \in [-T, 3T]$, T being a characteristic time interval. In detail, three events are simulated (figure 2):

at $t = 0$: as a consequence of an inflammatory process in the tissue, the infiltration of macrophages in the adventitia determines an increase in the production of ILs [60,61];

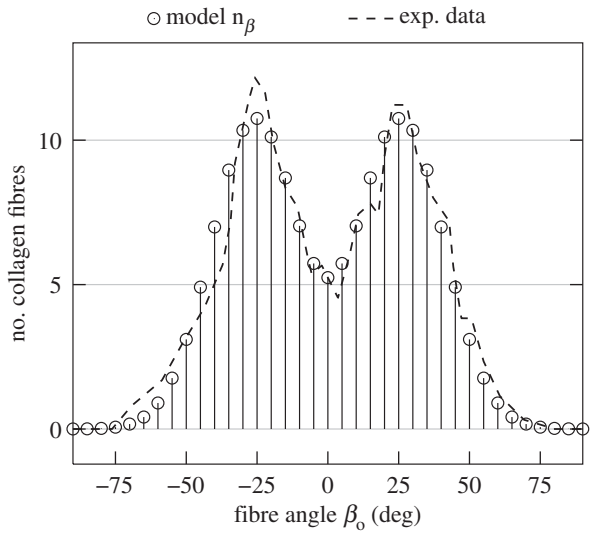

Figure 3. Circular distribution of the mean number of collagen fibres, occurring along the arterial thickness, versus the fibre angle β_o at homeostasis: experimental data derived from [54]; function $n_\beta(\beta_o)$ (assigned as an initial condition) is obtained from equation (5.22), employing function $v_c(\beta_o, \hat{\beta}_F, \bar{\mu}_F)$ (see equation (5.21)). Values $\bar{\mu}_F$ and $\pm\hat{\beta}_F$ can be found, respectively, in tables 3 and 4.

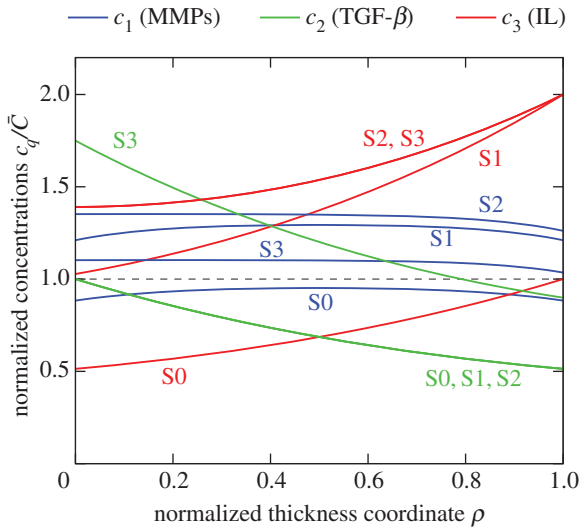

Figure 4. Normalized concentration profiles $c_q/\bar{C}$ versus normalized thickness coordinate ρ along the stages S0–S3 of the phsyiopathological mechanism ($q = 1, 2, 3$); the black dashed line denotes the threshold value corresponding to the activation of remodelling. Coordinates $\rho = 0$ and $\rho = 1$ correspond to the intima–media and media–adventitia interfaces, respectively. Remodelling thresholds $C_{R1} = C_{R2} = \bar{C}$.

at $t = T$: the pre-existing inflammatory condition couples with the thickening of the tunica intima which, in turn, determines a reduced intima permeability [18,19];

at $t = 2T$: as a consequence of possible autoimmune mechanisms or pharmacological treatments, the production of TGFs-β by endothelial cells in the intima increases [20].

Therefore, four temporal intervals, corresponding to different stages of the entire physiopathological mechanism, can be recognized: S0 for for $t \in [-T, 0)$, S1 for $t \in [0, T)$, S2 for $t \in [T, 2T)$ and S3 for $t \in [2T, 3T]$. As initial conditions, basal cellular activity and homeostatic tissue structure are assumed at $t = -T$.

3. Results

For the sake of presenting results, the normalized thickness coordinate ρ is introduced, where $\rho = 0$ corresponds to the intima–media interface and $\rho = 1$ to the media–adventitia one. Moreover, the through-the-thickness average values $s_j^{av}(t)$ are introduced for analysing the variation of the structural features s_j due to remodelling.

Two additional auxiliary quantities are function $r_i^{100}(t)$, i.e. the time-evolution of the internal radius r_i^{100} at the physiological pressure $P_i = 100$ mmHg, and function $n_\beta(\beta_o)$, i.e. the along-the-thickness mean number n_β of collagen fibres inclined by β_o with respect to the arterial circumferential direction. The latter function is affected by the dispersion of fibre orientation, measured by μ_F, and hence it generally varies with remodelling. The distribution of fibre orientation assigned at homeostasis (i.e. obtained with the reference value $\bar{\mu}_F$) is shown in figure 3 and compared with experimental data in [54]. The occurrence of two well-defined experimental preferred directions at $\beta_o = \pm\hat{\beta}_F \approx \pm 25°$ justifies the adopted circular bimodal distribution. Readers may refer to §5.6.1 for more details on model parameter calibration.

3.1. Homeostatic state: stage S0

As shown in figure 4, the obtained steady concentration profile c_1 (respectively, c_3) highlights that TGFs-β (respectively, ILs) diffuse in the media layer starting from the source at the intima–media interface for $\rho = 0$ (respectively, at the media–adventitia interface for $\rho = 1$). In turn, the resulting concentrations of TGFs-β and ILs at the homeostatic state determine a symmetric concentration profile of MMPs (i.e. c_1) with the maximum value at $\rho = 0.5$.

Based on the obtained solution of the transport problem, a null remodelling is predicted because it results $c_1 \leq C_{R1}$ and $c_2 \leq C_{R2}$. Therefore, the values of all structural features do not change with respect to the homeostatic state (as shown in figure 5 for $t \in [-T, 0]$ in terms of average values s_j^{av}). Accordingly, both constitutive properties and arterial mechanical response are constant in time, leading to the pressure–radius relationship shown in figure 6 for $t = 0$.

The predicted arterial compliance fully agrees with available experimental data reported in [58]. This proves the effectiveness of the present approach in capturing a realistic mechanical behaviour of thoracic aortic segments. It is worth noting that the same would be obtained for lower TGFs-β and ILs basal production.

3.2. Macrophage infiltration: stage S1

An increased activity of macrophages induces a higher source of ILs with respect to S0 from the adventitial layer, and thereby a higher concentration of ILs in the tunica media (figure 4). Clearly, in agreement with equation (2.1), TGFs-β are unaffected. Accordingly, the source term for MMPs increases, resulting in increased values of c_1 with respect to the homeostasis.

MMP concentration overrides the threshold concentration level, thereby inducing remodelling (i.e. $c_1 > C_{R1}$). Such an occurrence leads to a progressive degradation of tissue constituents, as shown in figure 5 in terms of average values s_j^{av}. Owing to a non-homogeneous remodelling

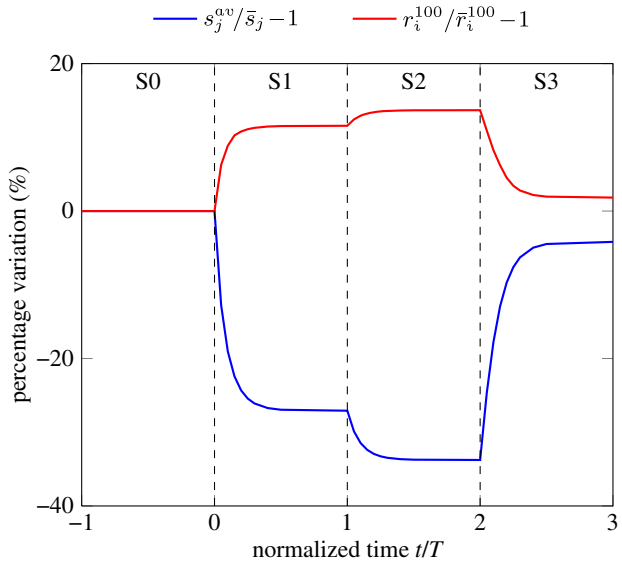

Figure 5. Percentage variation of the average values s_j^{av} of the structural features in arterial thickness (see equation (2.2)) and internal radius r_i^{100} at $P_i = 100$ mmHg versus the normalized time t/T. Values are normalized with respect to the values $\bar{s}_j$ and $\bar{r}_i^{100}$ attained at homeostasis (i.e. at $t = -T$). Time intervals of stages S0–S3 of the physiopathological mechanism herein modelled are also indicated.

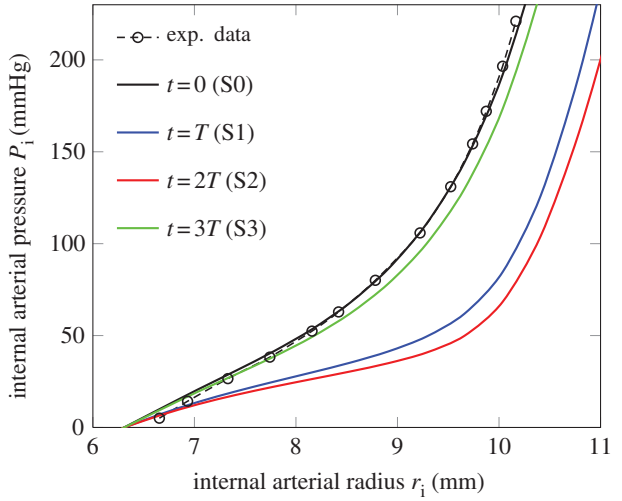

Figure 6. Internal pressure P_i versus internal radius r_i at $t = 0$, T, $2T$ and $3T$, corresponding to steady states of the remodelling mechanisms occurring at the stages S0–S3 of the physiopathological mechanism herein modelled. Experimental data from [58] on the compliance properties of thoracic aortic segments (where the tunica adventitia has been excised) are reported as benchmark for the homeostatic case (S0).

stimulus, the values of structural features become non-uniform in space, with a normalized difference between minimum and maximum values of s_j within the media after the remodelling of approximately 10% (figures 7 and 8). In fact, since MMP concentration is higher in the central region of the arterial thickness, elastin and collagen volume fractions, intermolecular cross-links density and fibre radius decrease with a minimum at $\rho = 0.5$ (figure 7), while the standard deviation measure μ_F of fibre orientation distribution increases with a maximum at $\rho = 0.5$ (figure 8). For the sake of clarity, the evolution of the corresponding circular distribution of the average number n_β of collagen fibres versus the fibre angle β_o is reported in figure 8. Therefore, it appears that the remodelling mechanism induces a more isotropic fibre distribution with respect to the homeostatic state, with the number of fibres along the preferred directions $\pm\hat{\beta}_F \approx \pm 25^\circ$ decreasing up to 40%.

As a result of the simulated remodelling process, arterial mechanics is significantly affected. The corresponding time-dependent pressure–radius relationship is reported in figure 9. As a matter of fact, figure 5 shows that the internal radius r_i^{100} at the physiological pressure of $P_i = 100$ mmHg enlarges at the steady state (for $t = T$) by approximately 10% with respect to the homeostatic case.

3.3. Intimal thickening: stage S2

The reduced permeability of the tunica intima, induced by intimal thickening, significantly affects the solution of the transport problem for ILs. Although IL source term is unaffected (the production by macrophages in the adventitia is the same as the one in stage S1), IL concentration increases in the tunica media (figure 4). This outcome yields further degradation of constituents (see figure 5 for $t \in [T, 2T]$) and thereby, from a mechanical point of view, further aortic enlargement (see curve P_i versus r_i in figure 6 at the end of stage S2, i.e. at $t = 2T$). In particular, as shown in figure 5, radius r_i^{100} enlarges by approximately 15% with respect to the homeostatic state.

3.4. Healing mechanism: stage S3

The increased activity of endothelial cells is reflected in an increased concentration of TGFs-β in the tunica media, which counterbalance the high IL concentration in the production of MMPs. Therefore, MMP concentration significantly decreases with respect to stage S2 (figure 4). Consequently, due to the lower amount of MMPs and the increased amount of TGFs-β (i.e. $c_2 > C_{R2}$), a healing process is triggered and the value of structural features tends towards the homeostatic value (see figure 5 for $t \in [2T, 3T]$). Therefore, as shown in figure 6, the physiological homeostatic arterial compliance behaviour is almost recovered at the end of stage S3 (i.e. at $t = 3T$). For instance, at $P_i = 100$ mmHg, the healing mechanism allows to recover approximately 7% of aortic enlargement and r_i^{100} is only 3% larger than the one at the homeostatic state S0 (figure 5).

4. Discussion and conclusion

The aim of the present work has been to develop an effective strategy for describing arterial physiopathological remodelling associated with alterations in tissue biochemical environment. The proposed model gathers a multiscale constitutive description of arterial tissues (that allows to account for main histological and biochemical properties of collagen [47–53]) together with a mechanistic modelling of cell–cell signalling pathways (involving molecular transport phenomena in the arterial thickness [33,34]). In turn, molecular pathways drive biochemically motivated remodelling laws of tissue structural features, and hence affect arterial mechanics, possibly determining the imbalance from the homeostasis.

With respect to the existing approaches [22–31], the employed strategy allows us to predict arterial chemo-mechano-biological response from a novel and unexplored perspective, where local, non-homogeneous and fine variations of histological and biochemical properties can be accounted

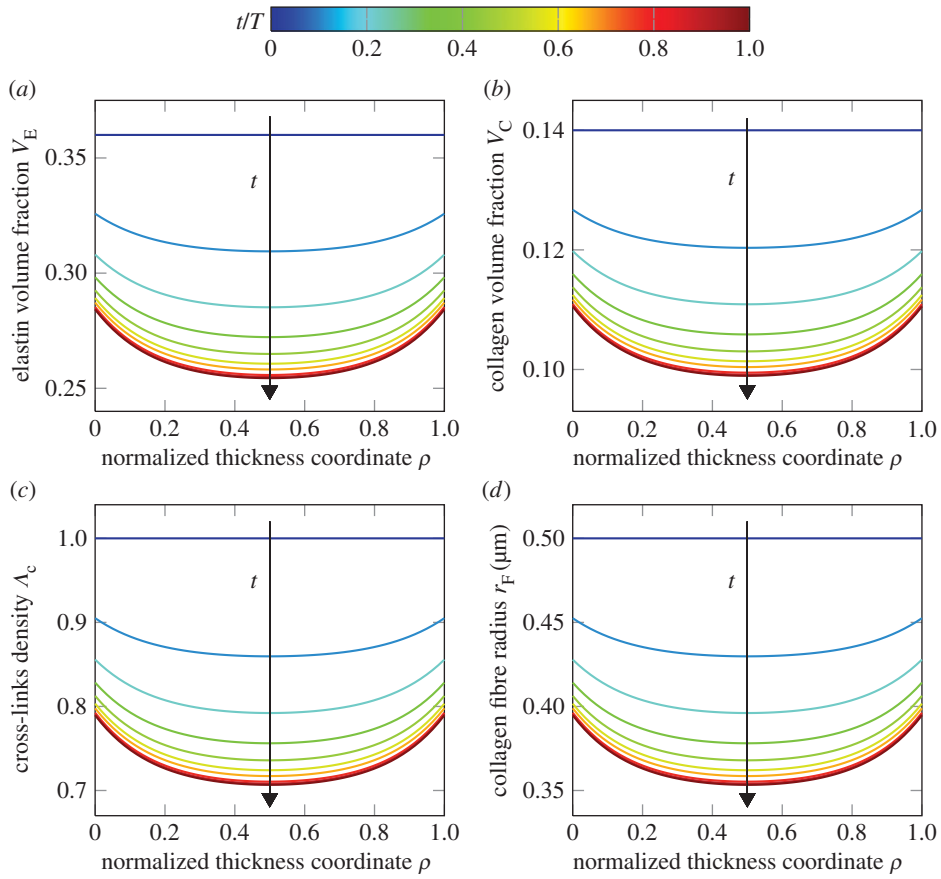

Figure 7. Stage S1: evolution of elastin volume fraction V_E (*a*), collagen volume fraction V_C (*b*), cross-links density Λ_c (*c*) and collagen fibre radius r_F (*d*) versus normalized thickness coordinate ρ. Colour map denotes different values of time $t \in [0, T]$; the time interval between curves is 0.1 *T*.

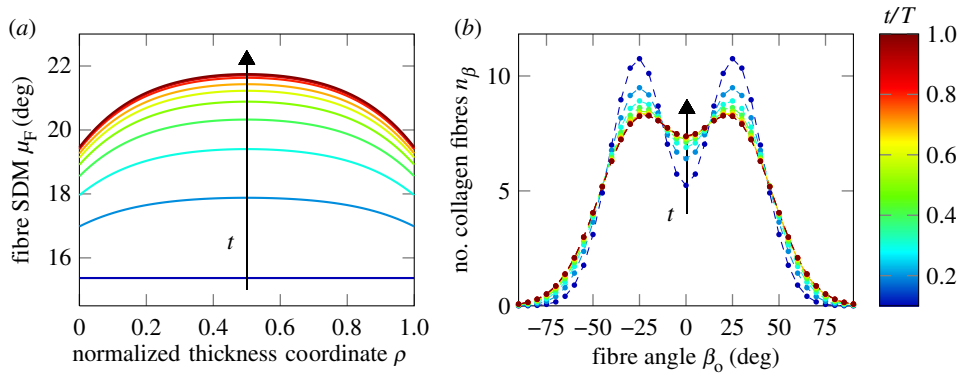

Figure 8. Stage S1: evolution of the orientation of collagen fibres. (*a*) Standard deviation measure (SDM) μ_F of collagen fibre orientation distribution versus normalized thickness coordinate ρ. (*b*) Circular distribution of the mean number n_β of collagen fibres, occurring along the arterial thickness, versus the fibre angle β_o. Colour map denotes different values of time $t \in [0, T]$; the time interval between curves is 0.1*T*.

for. As a matter of fact, even addressing very recent and refined chemo-mechano-biological modelling frameworks, such as the one proposed in [25], available approaches do not account for molecular reactive–diffusive transport mechanisms and describe tissue constitutive nonlinear response by means of a phenomenological form of the strain energy density associated with collagen fibres. On the contrary, the present paper highlights the key role of alterations in tissue constitutive behaviour, as well as diffusivity/permeability properties, in the non-functional macroscale mechanical response experienced during pathological events. These aspects are often overlooked with respect to the effects of mass/density changes.

Numerical results have been obtained by addressing a case study which shows the effects of ECM remodelling, induced by intra-arterial-wall transport of MMPs, TGFs-β and ILs, on the compliance of an axisymmetric arterial segment. Remarkably, addressing an inflammation mechanism described by the increased production of cytokines by macrophages, the model predicts that the proteolytic activity of MMPs induces an aortic enlargement of approximately 10%. This outcome fully agrees with clinical evidence that recognizes the key role of macrophages and MMPs in mediating ECM degradation during aneurysm formation [10,18]. Moreover, obtained results indicate that intimal thickening turns to be a complication which

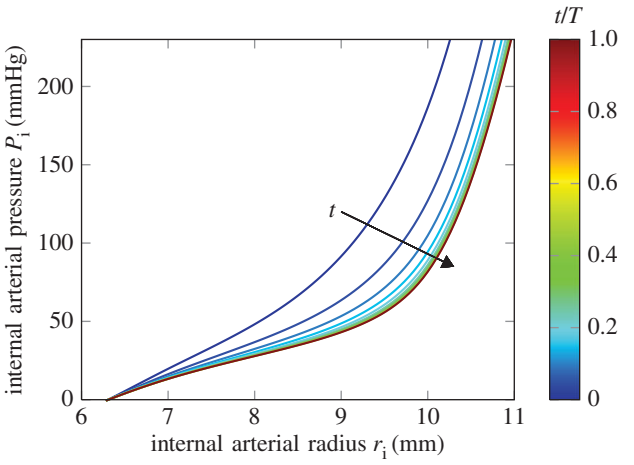

Figure 9. Stage S1: evolution of pressure–radius relationships, P_i versus r_i. Colour map denotes different values of time $t \in [0, T]$; the time interval between curves is 0.1 T.

promotes further aortic dilation (that reaches up to 15% with respect to the homeostatic case in the proposed application), in agreement with clinical data that correlate hyperplastic neointima formation and atherosclerotic plaques with aneurysmal development [18,19]. Furthermore, model results predict that aortic dilatation reduces to only 3% when MMP activity is counterbalanced by TGFs-β. This further outcome also agrees with evidence on the protective role of TGFs-β, the increased production of which might represent an autoimmune mechanism or be a consequence of a pharmacological treatment [20].

Future studies will address some limitations of the present work that can be straightforwardly incorporated by means of well-established approaches: the active contraction of SMCs and the unsteady effects due to fluid–structure interaction have not been considered [26,62]; possible damage and repair of ECM constituents have been neglected [24]; the mass growth and the natural turnover of ECM constituents have not been addressed [28,29], making it impossible to analyse ageing mechanisms, such as collagen production in response to progressive elastin lost [63]; no distinction has been made between latent and active concentrations or between pro- and anti-inflammatory forms of molecular species [25]; arterial geometry is idealized and only the media layer is addressed [32,64]; and the dispersed distribution of collagen fibres in tissues is simplified with respect to recent evidence on non-symmetric distributions [65,66].

Furthermore, no mechanical feedback in the transport problem has been introduced, arterial multiphysics response being reduced to an open-loop coupled system, in which the transport problem affects mechanics but not vice versa. General modelling strategies to overcome this limitation have been addressed in [21], but this is surely an open issue that merits significant efforts in the future. Analogously, remodelling might alter tissue diffusivity and permeability properties, forming a further feedback loop (of remodelling on transport) that should be accounted for. Furthermore, the mutual interaction of chemical and mass fluxes, as well as inelastic mechanisms associated with growth and remodelling, shall be considered within a general theoretical framework able to describe the thermodynamics of living systems, and thereby able to rigorously discuss the thermodynamic balance of the coupled formulation [67–70]. Finally, more data on the reactive–diffusive properties of molecular species, as well as on the cellular activity, are much needed in order to increase the quantitative reliability of obtained results.

5. Material and methods

5.1. Modelling assumptions

An artery-like structure is addressed as an illustrative example, representing an instructive case study aiming to capture the main mechanisms under investigation by means of an analytical solution. The main assumptions are summarized in the following (figure 2).

— The reference (stress-free and load-free) configuration is a hollow open cylinder with internal radius $r_{i,o}$, external radius $r_{e,o}$ and opening angle α. The (stressed and loaded) current configuration corresponds to a hollow closed cylinder with internal r_i and external r_e radii and described by a cylindrical coordinate system.
— A uniform internal pressure P_i is applied to the inner surface of the cylinder. It is worth highlighting that, due to the pulsatile nature of blood flow, the applied pressure should indeed be non-uniform. Nevertheless, the uniform applied pressure can be regarded as the corresponding average measure along the cardiac cycle, so that the resulting mechanical quantities are, in turn, time-averaged values, in agreement with the aim of investigating possible variations of quasi-static arterial compliance.
— Tissue is characterized by an anisotropic mechanical response due to the presence of collagen fibres, lying on cylindrical surfaces coaxial with the arterial segment and being arranged along multiple directions. The circular distribution of fibres' orientation is assumed to be bimodal and symmetric with respect to the circumferential direction, the latter being close to the peak angles of the distribution. Therefore, material behaviour results orthotropic, with symmetry axes aligned with the basis of the cylindrical coordinate system. Moreover, fibre arrangement, and thereby material response, is assumed to be independent from the circumferential coordinate.
— Concentration c_q of each molecule in the tissue is obtained from a reactive–diffusive transport problem formulated by considering a constant diffusivity tensor $\mathbf{D}_q$. The latter describes an anisotropic diffusion, with principal directions aligned with the basis of the cylindrical coordinate system [32]. The variation of cylinder thickness $\delta = r_e - r_i$ is neglected in the solution of the transport problem, assuming $\delta \approx \delta_o = r_{e,o} - r_{i,o}$. Transport boundary conditions are constant in space, with null flux through cylinder end cross sections.

Under the present assumptions, the problem is planar in the cylinder cross-section plane and axisymmetric. Hence, all variables in the current configuration spatially depend (at most) only on the radial coordinate, denoted by $r \in [r_i, r_e]$ in the current configuration and associated with the positions identified by $r_o \in [r_{i,o}, r_{e,o}]$ in the reference configuration. Therefore, let $\rho = (r_o - r_{i,o})/\delta_o$ be the dimensionless radial coordinate, such that $\rho = 0$ and $\rho = 1$ correspond to the inner and outer surfaces, respectively, in the reference configuration. Despite significant simplifying assumptions, the cylindrical segment can be regarded as representative of the tunica media, the latter being addressed due to its key role on arterial compliance properties. Therefore, surfaces at $\rho = 0$ and $\rho = 1$ can be retained as representative of the intima–media and of the media–adventitia interfaces, respectively.

As notation rules, first- and second-order tensors are indicated, respectively, in lowercase and uppercase bold-face, while scalars are indicated as normal-face. Determinant, transpose and trace of a second-order tensor $\mathbf{A}$ are denoted, respectively, by $\mathrm{Det}(\mathbf{A})$, $\mathbf{A}^T$ and $\mathrm{Tr}(\mathbf{A})$. Symbol $\otimes$ denotes tensor product and the diagonal matrix with entries a, b and c is given by

Diag(a, b, c). Finally, symbols ∂ and d correspond to partial and total derivatives.

Moreover, as subscripts and indexes rules (see §2.1), q denotes different molecules and ranges over $1, 2, 3$; j refers to the structural features undergoing remodelling and ranges over $1, \ldots, 5$; k indicates different stages of the addressed physiopathological mechanism and takes values in $0, \ldots, 3$.

5.2. Modelling framework

Let $\mathbf{F}$ be the deformation gradient associated with arterial mapping from the reference to the current configuration. In the framework of a constrained mixture approach [22,23], each volume element is regarded as a constrained mixture of two constituents: collagen fibres (subscript C) and non-collagenous matrix (e.g. elastin and SMCs, subscript M). As an index rule, subscript i takes values in $\{C, M\}$.

Different deposition/resorption times of constituents during growth and remodelling lead to different stress-free states of each constituent. In this framework, Cyron *et al*. [22,23] formulated a homogenized constrained mixture approach by introducing deformation gradients $\mathbf{F}_i$ of individual constituents, multiplicatively split in (i) inelastic contributions $\mathbf{F}_i^{gr}$, that allow us to capture growth/resorption associated with a change in tissue mass and to consider remodelling due to mass turnover, and (ii) elastic contributions $\mathbf{F}_i^{e}$, required to assemble the individual constituents into a contiguous body and to describe the subsequent deformation associated with external loads. Owing to compatibility, the total deformation gradient $\mathbf{F}$ coincides with one of the different constituents $\mathbf{F}_i$, namely

$$\mathbf{F} = \mathbf{F}_C^{e}\mathbf{F}_C^{gr} = \mathbf{F}_M^{e}\mathbf{F}_M^{gr}. \tag{5.1}$$

Owing to high water content, arterial tissues are typically modelled as incompressible materials. Therefore, elastic deformations are supposed to be isochoric, that is $\mathrm{Det}(\mathbf{F}_i^{e}) = 1$ [23].

The second Piola–Kirchhoff stress $\mathbf{S} = 2\partial\Psi_T/\partial\mathbf{C}$ is computed from the (volume-specific) strain energy density function Ψ_T. The latter depends on the Cauchy–Green deformation tensor $\mathbf{C} = \mathbf{F}^{T}\mathbf{F}$ via the constituent-specific elastic right Cauchy–Green tensors $\mathbf{C}_i^{e} = (\mathbf{F}_i^{e})^{T}\mathbf{F}_i^{e}$. Moreover, in order to account for the effects of remodelling on the constitutive response, the explicit dependence on the set $\mathcal{S}$ of structural features introduced in equation (2.2) is highlighted, namely:

$$\Psi_T = \Psi_T(\mathbf{C}_C^{e}, \mathbf{C}_M^{e}, \mathcal{S}). \tag{5.2}$$

Although the authors are aware of the instrumental role of mass/density changes, it is recalled that the present paper aims to highlight the role of remodelling-induced tissue constitutive response. Therefore, within the limitations of the proposed formulation and in order to isolate the effects under investigation, the present paper does not address mass turnover and growth, for which the reader can refer to the literature [22–31,67–70]. In detail, the variation of the mechanical response due to alterations in the stress-free reference configuration of the single constituents is not accounted for, assuming that inelastic contributions to the deformation gradients remain equal to the identity, that is $\mathbf{F}_i^{gr} = \mathbf{I}$. It is worth highlighting that, in the present framework,

$$\mathrm{Det}(\mathbf{F}) = \mathrm{Det}(\mathbf{F}_i^{e}) = 1 \tag{5.3}$$

and hence constitutive incompressibility corresponds to null changes in the total volume. Such an assumption is surely an explicit violation of real processes [70] but it is adopted in the light of the scope of present application which aims to isolate the effects of fine remodelling mechanisms on macroscale behaviour.

Tissue biochemical environment is determined from the solution of a molecular transport problem T which gives the concentration of biologically active molecules, collected in vector $\mathbf{c}$. The latter drives remodelling laws R, and thereby the value of structural features $\mathcal{S}$. The altered structure of tissues affects their constitutive response (see equation (5.2)), and thereby arterial macroscale mechanics M. In particular, a multiscale homogenization approach allows to introduce the explicit dependence of Ψ_T on $\mathcal{S}$.

Moreover, the principle of separation of time scales is employed: remodelling occurs within characteristic time intervals (i.e. months to years) larger than the ones of transport (i.e. hours to days), in turn, larger than the ones of mechanics (i.e. seconds even accounting for pulsatile blood flow). The time variable t is introduced as comparable with the time scale of remodelling.

Owing to the separation of time scales and since the solution of the transport problem T is here adopted for obtaining the stimulus driving remodelling, problem T is conveniently solved under steady-state assumptions in each physiopathological stage (from S0 to S3, see §2.1). As a matter of fact, under constant boundary conditions, transport problem leads to a steady state which is physically reached within a time length much lower than the remodelling characteristic time T.

Therefore, T is formulated as steady, by enforcing boundary conditions as constant for $t \in T_k = [(k-1)T, kT]$, but different for different values of k (namely, different for each stage from S0 to S3). Accordingly, the biochemical quantities affecting problem R within the time interval T_k are assumed to be represented by the corresponding steady-state concentrations $\mathbf{c}$ computed from T.

Within each time interval $t \in T_k$, the solution strategy is as follows:

1. the steady-state transport problem T is solved, obtaining $\mathbf{c} = \mathbf{c}(r)$, see §5.3;
2. tissue biochemical environment $\mathbf{c}(r)$ drives the remodelling R of tissue structure, leading to $\mathcal{S} = \mathcal{S}(r,t)$, see §5.4;
3. the remodelling of tissue structure affects arterial mechanics M, obtained in terms of compliance, that is by referring to the function $P_i = P_i(r_i, t)$, see §5.5.

5.3. Molecular transport

Following the evidence stated in equation (2.1) addressed in the present case study (figure 2), problem T is defined, analogously to [32–37], as

$$\underbrace{\frac{D_1^{r}}{\delta_o^2}\frac{\partial^2 c_1}{\partial \rho^2}}_{\text{diffusion}} + \underbrace{\eta_{13} V_S \overbrace{R^{+}(c_3)}^{\text{ILs}} \overbrace{(C_{sat} - c_1)}^{\text{saturation}}}_{\text{source}} - \underbrace{[\overbrace{\zeta_1}^{\text{decay}} + \eta_{12} V_S \overbrace{R^{-}(c_2)}^{\text{TGFs-}\beta}]c_1}_{\text{consumption}} = 0 \tag{5.4a}$$

and

$$\underbrace{\frac{D_v^{r}}{\delta_o^2}\frac{\partial^2 c_v}{\partial \rho^2}}_{\text{diffusion}} - \underbrace{\zeta_v c_v}_{\text{consumption (decay)}} = 0 \quad \text{with } v = 2,3, \tag{5.4b}$$

where D_q^{r} is the radial component of tensor $\mathbf{D}_q$ (see §5.1). The production and degradation of MMPs is driven by TGFs-β and ILs by introducing functions $R^{-}(c_2)$ and $R^{+}(c_3)$, respectively. Functions $R^{\pm}(c_v)$ are defined on the basis of a linear relationship governed by the across-the-thickness average concentrations c_v^{av} of TGFs-β ($v = 2$) and ILs ($v = 3$), that is $R^{\pm}(c_v) = c_v^{av}/\gamma_v$. Here, γ_v are stimulative concentration values that correspond to a unitary remodelling stimulus, that is such that $R^{\pm} = 1$ when $c_v^{av} = \gamma_v$. Moreover, these terms are scaled with the volume fraction V_S of SMCs, because these pathways are mediated by SMCs. Furthermore, constants η_{1v} govern the kinetics of source/consumption of MMPs (c_1) from concentration c_v, i.e. represent reaction kinetics rate constants.

To account for natural molecular degradation, a linear decay term, regulated by the proportionality constant ζ_q, is also accounted for. Finally, aiming to describe saturation effects,

the source of MMPs by SMCs is scaled with the difference between the MMP concentration c_1 at hand and the saturated concentration C_{sat}.

Equations (5.4*a*) and (5.4*b*) are completed by the following boundary conditions:

$$\text{at } \rho = 0: \begin{cases} \dfrac{\partial c_1}{\partial \rho} = \dfrac{\delta_o \hat{\lambda}_{i,1}}{D_1^r} c_1 \\ c_2 = \hat{c}_2 \\ \dfrac{\partial c_3}{\partial \rho} = \dfrac{\delta_o \hat{\lambda}_{i,3}}{D_3^r} c_3 \end{cases} \qquad \text{at } \rho = 1: \begin{cases} \dfrac{\partial c_1}{\partial \rho} = -\dfrac{\delta_o \hat{\lambda}_{e,1}}{D_1^r} c_1 \\ \dfrac{\partial c_2}{\partial \rho} = -\dfrac{\delta_o \hat{\lambda}_{e,2}}{D_2^r} c_2 \\ c_3 = \hat{c}_3. \end{cases} \tag{5.4c}$$

Here, $\hat{\lambda}_{i,q}$ and $\hat{\lambda}_{e,q}$ are molecule-specific apparent permeabilities of the intima and of the adventitia, respectively [36]. Moreover, in order to mimic the presence of macrophages (respectively, endothelial cells), a constant source of ILs (respectively, TGFs-β) is modelled at the media–adventitia (respectively, intima–media) interface and associated with a given concentration level $\hat{c}_3$ (respectively, $\hat{c}_2$).

Equations (5.4) can be solved analytically. First, the independent equations (5.4*b*) are solved and the through-the-thickness average concentrations c_v^{av} are computed; then, the latter are employed for obtaining the solution of equation (5.4*a*). Accordingly,

$$c_1(\rho) = k_{11} \exp(-h_1 \rho) + k_{12} \exp(h_1 \rho) + \frac{A}{h_1^2} \tag{5.5a}$$

and

$$c_v(\rho) = k_{v1} \exp(-h_v \rho) + k_{v2} \exp(h_v \rho), \tag{5.5b}$$

where

$$A = \eta_{13} \delta_o^2 \frac{V_S c_3^{av} C_{sat}}{D_1^r \gamma_3}, \tag{5.5c}$$

$$h_1^2 = \frac{\delta_o^2}{D_1^r} \left(\zeta_1 + \eta_{12} \frac{V_S c_2^{av}}{\gamma_2} + \eta_{13} \frac{V_S c_3^{av}}{\gamma_3} \right) \tag{5.5d}$$

and

$$h_v^2 = \frac{\delta_o^2 \zeta_v}{D_v^r}, \tag{5.5e}$$

and constants k_{q1} and k_{q2} are determined from boundary conditions in equation (5.4*c*).

5.4. Remodelling laws

Inspired by applications in biology, chemistry, medicine and biomathematics [71], as well as in agreement with experimental evidence on ECM remodelling [72], the functional form $s_j(\rho, t)$ in each physiopathological stage S*k* is assumed to be described by a logistic function centred in $t = (k-1)T$ and characterized by steepness ν_j^{-1}. In particular, ν_j has the dimension of a time and it governs the tissue resistance to remodelling of structural feature s_j. Therefore, it can be referred to as a remodelling viscosity. The remodelling laws are defined in a way that s_j asymptotically tends towards the target value $\bar{s}_j + \mathcal{I}_j(\mathbf{c})$ for $t \gg \nu_j$, that is [71]:

$$s_j(\rho, t) = \frac{s_j^o(\rho)[\bar{s}_j + \mathcal{I}_j(\mathbf{c})] \exp(t/\nu_j)}{\bar{s}_j + \mathcal{I}_j(\mathbf{c}) + s_j^o(\rho)[\exp(t/\nu_j) - 1]}, \tag{5.6}$$

where $s_j^o(\rho) = s_j(\rho, (k-1)T)$. The homeostatic imbalance $\mathcal{I}_j(\mathbf{c})$ depends only on MMPs (c_1) and TGFs-β (c_2) concentrations, and it is defined by following the additive decomposition $\mathcal{I}_j(\mathbf{c}) = \mathcal{I}_j^-(c_1) + \mathcal{I}_j^+(c_2)$. In agreement with the evidence in equation (2.3) and with the schematic in figure 2, it results in $\mathcal{I}_j^-(c_1) < 0$ when $c_1 > C_{R1}$ (and zero otherwise) and $\mathcal{I}_j^+(c_2) > 0$ when $c_2 > C_{R2}$ (and zero otherwise), that is:

$$\mathcal{I}_j^-(c_1) = -\frac{\bar{s}_j \langle c_1(\rho, t) - C_{R1} \rangle}{C_{R1}} \tag{5.7a}$$

and

$$\mathcal{I}_j^+(c_2) = \frac{\bar{s}_j V_S \langle c_2(\rho, t) - C_{R2} \rangle}{C_{R2}}, \tag{5.7b}$$

with $\langle x \rangle = (x + |x|)/2$ denoting the Macaulay brackets.

For the physical admissibility of the values of s_j obtained from equations (5.6), the following constraints for any $\rho \in [0, 1]$ and for any time t are enforced:

$$r_F(\rho, t) > 0, \quad \Lambda_c(\rho, t) > 0 \quad \text{and} \quad \mu_F(\rho, t) > 0 \tag{5.8a}$$

and

$$\frac{d}{dt}(V_C(\rho, t) + V_C^0(\rho, t)) = 0 \quad \text{and}$$
$$\frac{d}{dt}(V_E(\rho, t) + V_E^0(\rho, t)) = 0, \tag{5.8b}$$

where $V_E^0(\rho, t)$ and $V_C^0(\rho, t)$ represent the volume fractions of elastin and collagen in a structural form which is non-functional from the mechanical point of view (e.g. fragmented elastin, degraded collagen).

Neglecting possible variations of constituents' density with the structural form (i.e. between mechanically functional and non-mechanically functional forms) and under the incompressibility assumption (see equation (5.3)), relationships in equations (5.8*b*) correspond to enforcing a constant mass of constituents along the physiopathological mechanism. As previously highlighted (see §5.2), this choice agrees with the aim of investigating only the effects of remodelling in terms of alterations of tissue strain energy function.

5.5. Mechanics

Arterial deformation is described by the right Cauchy–Green deformation tensor $\mathbf{C} = \mathrm{Diag}(\lambda_r^2, \lambda_\theta^2, \lambda_z^2)$, where λ_r, λ_θ and λ_z are stretches in the radial, circumferential and axial direction, respectively. In agreement with the opening angle method [39,41] and assuming a constant axial stretch λ_z, the incompressibility condition (see equation (5.3)), that is:

$$\lambda_r \lambda_\theta \lambda_z = 1, \quad 2\pi r \lambda_r \lambda_z = (2\pi - \alpha) r_o, \tag{5.9}$$

gives

$$\lambda_r = \lambda_r(r) = \frac{r_o(r)}{\kappa \lambda_z r}, \quad \lambda_\theta = \lambda_\theta(r) = \frac{\kappa r}{r_o(r)}, \tag{5.10}$$

where $\kappa = 2\pi/(2\pi - \alpha)$ accounts for the opening angle α. Function $r_o = r_o(r)$, defined as

$$r_o = r_o(r) = \sqrt{\kappa \lambda_z (r^2 - r_i^2) + r_{i,o}^2}, \tag{5.11}$$

correlates the radial position $r \in [r_i, r_e]$ of a material point in the current configuration with the one $r_o \in [r_{i,o}, r_{e,o}]$ in the reference configuration.

The following equilibrium relationship holds between luminal pressure P_i and internal radius r_i [39,41]:

$$P_i = P_i(r_i, t) = \int_{r_i}^{r_e(r_i)} [\sigma_\theta(r, t) - \sigma_r(r, t)] \frac{dr}{r}, \tag{5.12}$$

where $r_e(r_i) = [r_i^2 + (r_{e,o}^2 - r_{i,o}^2)/(\kappa \lambda_z)]^{1/2}$ (see equation (5.11)), and σ_r and σ_θ are Cauchy stress components in the radial and circumferential directions, respectively. The latter are given by (see equation (5.2))

$$\sigma_\theta = \sigma_\theta(r, t) = \lambda_\theta(r) \frac{\partial}{\partial \lambda_\theta} \Psi_T(\mathbf{C}_C^e, \mathbf{C}_M^e, \mathcal{S}(r, t)) \tag{5.13a}$$

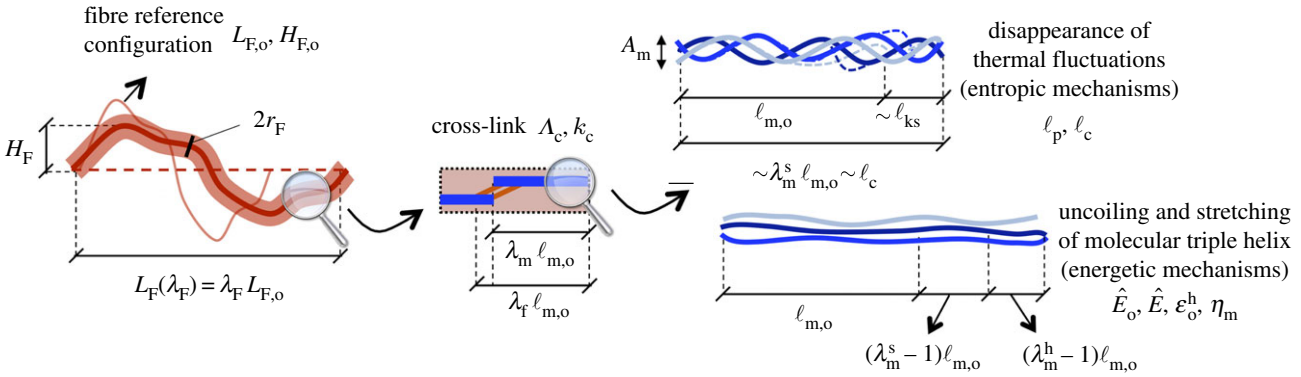

Figure 10. Multiscale constitutive approach: schematic of stretch measures and structurally motivated parameters for the derivation of the equivalent tangent modulus C_F of crimped collagen fibres (see §5.5.1 and appendix A). As inelastic deformation associated with growth and remodelling is neglected in the present modelling framework (see §5.2), the figure is represented under the assumption that elastic fibre stretch λ_F^e corresponds to the total fibre stretch λ_F, namely $\lambda_F^e = \lambda_F$.

and

$$\sigma_r = \sigma_r(r,t) = \lambda_r(r)\frac{\partial}{\partial \lambda_r}\Psi_T(\mathbf{C}_C^e, \mathbf{C}_M^e, \mathcal{S}(r,t)). \tag{5.13b}$$

Radial- and time-dependency of Cauchy stresses in equations (5.13) follow from the radial- and time-dependency of structural features in $\mathcal{S}$ (i.e. from remodelling laws). In particular, function $\mathcal{S} = \mathcal{S}(r,t)$ is obtained from $s_j(\rho,t)$ in §5.4 with $\rho(r) = (r_o(r) - r_{i,o})/\delta_o$ (see equation (5.11)). The time-dependency of the pressure–radius relationship (5.12) immediately follows from the one of $\mathcal{S}(r,t)$. Clearly, when $\mathcal{S}$ reaches the steady state, the same occurs for function $P_i(r_i,t)$. The dependence of strain energy function Ψ_T on set $\mathcal{S}$ is derived via a multiscale approach described in the following §5.5.1.

5.5.1. Multiscale tissue constitutive description

Recalling that V_C (i.e. parameter s_2 in equation (2.2)), V_E (i.e. parameter s_1 in equation (2.2)) and V_S, respectively, represent the volume fraction of collagen fibres, elastin and SMCs, tissue strain energy density function Ψ_T (see equation (5.2)) is given by

$$\Psi_T(\mathbf{C}_C^e, \mathbf{C}_M^e, \mathcal{S}) = V_M \Psi_M(\hat{I}_{M1}^e) + V_C \int_{-\pi/2}^{\pi/2} \psi_C(\mathbf{C}_C^e, \mathbf{M}_o(\beta_o), \mathcal{S})\, d\beta_o, \tag{5.14}$$

where $V_M = V_E + V_S$, and terms Ψ_M and ψ_C are associated with non-collagenous and collagenous constituents, respectively. Introducing $\hat{I}_{M1}^e = [\mathrm{Det}(\mathbf{C}_M^e)]^{-1/3}\,\mathrm{Tr}(\mathbf{C}_M^e)$, a neo-Hookean approach for incompressible materials is employed for the strain energy term Ψ_M, that is:

$$\Psi_M(\hat{I}_{M1}^e) = k_M(\hat{I}_{M1}^e - 3). \tag{5.15}$$

Term ψ_C depends on the direction of collagen fibres via the structural tensor $\mathbf{M}_o = \mathbf{e}_{F,o} \otimes \mathbf{e}_{F,o}$, where the unit vector $\mathbf{e}_{F,o}$ identifies fibre direction in the reference configuration. Considering the fibre arrangement assumed in §5.1 and employing a cylindrical coordinate system, it results in $\mathbf{e}_{F,o} = (0, \cos(\beta_o), \sin(\beta_o))^T$, where β_o is the angle of an individual collagen fibre with respect to the circumferential direction in the reference configuration. Hence, the functional dependence $\mathbf{M}_o = \mathbf{M}_o(\beta_o)$ is highlighted. In particular, ψ_C is defined as

$$\psi_C(\mathbf{C}_C^e, \mathbf{M}_o(\beta_o), \mathcal{S}) = v_c(\beta_o, \hat{\beta}_F, \mu_F)\Psi_C(\lambda_F^e(\mathbf{C}_C^e, \beta_o), \mathcal{S}_F), \tag{5.16}$$

where Ψ_C is the strain-energy density of collagen fibres and v_c is the probability density function (PDF) of the orientation of collagen fibres. Function Ψ_C depends on set $\mathcal{S}_F = \{r_F, \Lambda_c\}$, collecting fibre structural features that are here assumed to undergo remodelling (see equation (2.2)), and on fibre elastic stretch λ_F^e, defined as

$$\lambda_F^e(\mathbf{C}_C^e, \beta_o) = [\mathrm{Tr}(\mathbf{C}_C^e \mathbf{M}_{gr}(\beta_o))]^{1/2}. \tag{5.17}$$

Here, $\mathbf{M}_{gr} = \mathbf{M}_{gr}(\beta_o)$ is the structural tensor obtained from the mapping of fibre direction $\mathbf{e}_{F,o}$ in the intermediate configuration reached by the inelastic contribution $\mathbf{F}_C^{gr}$, resulting in

$$\mathbf{M}_{gr}(\beta_o) = \frac{\mathbf{F}_C^{gr}\mathbf{M}_o(\beta_o)(\mathbf{F}_C^{gr})^T}{\mathrm{Tr}(\mathbf{C}_C^{gr}\mathbf{M}_o(\beta_o))}, \tag{5.18}$$

where $\mathbf{C}_C^{gr} = (\mathbf{F}_C^{gr})^T\mathbf{F}_C^{gr}$. Furthermore, function $v_c = v_c(\beta_o, \hat{\beta}_F, \mu_F)$ in equation (5.16) gives the probability of finding a fibre inclined by β_o. Recalling that fibre orientation follows a circular bimodal distribution, symmetric with respect to $\beta_o = 0$, the dependence on peak values at $\beta_o = \pm\hat{\beta}_F$ and on the standard deviation measure μ_F (i.e. parameter s_5^{-1} in equation (2.2)) is also highlighted.

The strain-energy density Ψ_C is defined by considering the mechanics of collagen fibres with a crimped microstructure and a nonlinear material behaviour. Fibres are regarded as periodic curvilinear beam structures. In this framework, elastic fibre stretch λ_F^e physically represents the along-the-chord extension of crimped fibres associated with an increment of the applied along-the-chord load. Therefore, fibre mechanics is described by introducing a stretch-dependent equivalent tangent modulus $C_F = C_F(\lambda_F^e, \mathcal{S}_F)$ which physically represents a measure of fibre stiffness along their main direction.

Since the inelastic deformation associated with growth and remodelling is here neglected (see §5.2), function $C_F(\lambda_F^e, \mathcal{S}_F)$ is obtained under the assumption that the elastic fibre stretch λ_F^e corresponds to the total fibre stretch $\lambda_F = [\mathrm{Tr}(\mathbf{C}_C\mathbf{M}_o)]^{1/2}$, namely $\lambda_F^e = \lambda_F$. In particular, by applying the principle of virtual works, the equivalent tangent modulus $C_F(\lambda_F^e, \mathcal{S}_F)$ is obtained as (dependences omitted) [50]

$$C_F = \frac{\ell_F^2 + H_F^2}{\sqrt{(L_{F,o}/4)^2 + H_{F,o}^2}}\left\{\left(\frac{1}{E_m} + \frac{A_m}{\Lambda_c k_c \ell_{m,o}}\right)\left[\ell_F + \frac{4H_F^2}{3r_F^2\ell_F}(\ell_F^2 + H_F^2)\right]\right\}^{-1}. \tag{5.19}$$

Here, $\ell_F = \ell_F(\lambda_F^e)$ and $H_F = H_F(\lambda_F^e)$ respectively represent the quarter-of-period and the amplitude of crimped fibres in the current configuration. Moreover, $E_m = E_m(\lambda_F^e)$ gives the tangent modulus of collagen molecules. These functions, nonlinearly depending on elastic fibre stretch, are determined from equilibrium and compatibility relationships, formulated following the multiscale homogenization approach presented in [47–49] within an updated-Lagrangian formulation, and extended in a total-Lagrangian framework in [50]. The multiscale rationale is schematically depicted in figure 10, while the employed analytical formulation

is reported in appendix A for the sake of completeness. Other parameters in equation (5.19) are fibre period $L_{\mathrm{F,o}}$ and amplitude $H_{\mathrm{F,o}}$ in the reference configuration, as well as fibre (constant) radius r_{F} (i.e. parameter s_3 in equation (2.2)); cross-sectional area A_{m} and reference length $\ell_{\mathrm{m,o}}$ of collagen molecules (mole fraction); density Λ_{c} of inter-molecular covalent cross-links (i.e. parameter s_4 in equation (2.2)) and their (constant) stiffness k_{c}.

In conclusion, the strain-energy density term Ψ_{C} is defined as

$$\Psi_{\mathrm{C}}(\lambda_{\mathrm{F}}^{\mathrm{e}}, \mathcal{S}_{\mathrm{F}}) = \int_1^{1+\langle\lambda_{\mathrm{F}}^{\mathrm{e}}-1\rangle} \int_1^{1+\langle\xi-1\rangle} \frac{C_{\mathrm{F}}(\eta, \mathcal{S}_{\mathrm{F}})}{\eta}\, \mathrm{d}\eta\, \mathrm{d}\xi. \tag{5.20}$$

Accounting for equations (5.14), (5.16) and (5.19), function $\Psi_{\mathrm{C}}(\lambda_{\mathrm{F}}^{\mathrm{e}}, \mathcal{S}_{\mathrm{F}})$ in equation (5.20) provides an analytical description of macroscale tissue mechanical properties as a function of geometric and material nonlinearities due to collagen fibres: the former due to the straightening of fibre crimp at microscale; the latter associated with intrafibre deformation mechanisms of cross-linked molecular assemblies at nanoscale (i.e. molecular elongation and sliding).

It is worth observing that, within the limitations of the present approach and in the framework of a homogenized constrained mixture formulation [22,23], tissue strain-energy density Ψ_{T} given in equation (5.14) represents the addition of strain-energy density contributions of constituents, where each energy part depends on the specific elastic right Cauchy–Green deformation tensor describing the corresponding constituent strain. Since this strain is, in general, different among different constituents, equation (5.14) does not correspond to considering elastin and collagen as acting as in a standard parallel scheme.

5.6. Application

In the case study addressed as application (see §2.1), the analysis of biochemical-induced physiopathological mechanisms is simulated by considering the alteration of the boundary conditions of the transport problem T (see equation (5.4*c*)). In particular, alterations in the production of TGFs-β ($\hat{c}_2$) and ILs ($\hat{c}_3$) with respect to basal productions $\hat{c}_2^{\mathrm{bas}}$ and $\hat{c}_3^{\mathrm{bas}}$ are considered as, respectively, associated with an increased activity of endothelial cells (e.g. due to a pharmacological treatment [20]) and of macrophages (e.g. due to inflammation [60,61]). Moreover, intima ($\hat{\lambda}_{\mathrm{i},q}$) and adventitia ($\hat{\lambda}_{\mathrm{e},q}$) apparent permeabilities vary with respect to physiological values $\hat{\lambda}_{\mathrm{i},q}^{\mathrm{ph}}$ and $\hat{\lambda}_{\mathrm{e},q}^{\mathrm{ph}}$, in order to address altered molecular wash-out (e.g. due to atherosclerotic plaques [18,19]).

For reproducing the physiopathological stages S0–S3 (see §2.1), the boundary conditions of the transport problem are varied as in table 1, such that an increase of $\hat{c}_2$ occurs at $t = 0$, a decrease of $\hat{\lambda}_i$ at $t = T$, an increase of $\hat{c}_3$ at $t = 2T$. The initial conditions at $t = -T$ for the time-dependent remodelling problem R correspond to a homeostatic state, that is $s_j = \bar{s}_j$ in the entire arterial domain. The characteristic time interval T of each stage S0 to S3 is chosen as $T = 1$ year, in order to be comparable with the time scale of the growth of aneurysms [73].

Addressing mechanics, an axial stretch $\lambda_z = 1$ is chosen in the numerical application. Moreover, the PDF $v_{\mathrm{c}}(\beta_{\mathrm{o}}, \hat{\beta}_{\mathrm{F}}, \mu_{\mathrm{F}})$ of the orientation of collagen fibres is chosen as a symmetric bimodal circular distribution obtained as the sum of two von Mises distributions with weights equal to $\frac{1}{2}$:

$$v_{\mathrm{c}}(\beta_{\mathrm{o}}, \hat{\beta}_{\mathrm{F}}, \mu_{\mathrm{F}}) = \frac{1}{4\pi\mathcal{I}_0(\mu_{\mathrm{F}}^{-2})} \left\{ \exp\left[\frac{\cos(\beta_{\mathrm{o}} - \hat{\beta}_{\mathrm{F}})}{\mu_{\mathrm{F}}^2}\right] + \exp\left[\frac{\cos(\beta_{\mathrm{o}} + \hat{\beta}_{\mathrm{F}})}{\mu_{\mathrm{F}}^2}\right] \right\}, \tag{5.21}$$

where $\mathcal{I}_0$ is the modified Bessel function of order 0. For the sake of simplicity, numerical results are obtained by considering the limiting behaviour of equation (5.21) for small variance.

Table 1. Boundary conditions of the transport problem T addressed in the numerical simulation and associated with physiopathological stages S0–S3 (see §2.1): TGF-β ($\hat{c}_2$) and ILs ($\hat{c}_3$) sources; apparent permeabilities of the intima ($\hat{\lambda}_{\mathrm{i},q}$) and of the adventitia ($\hat{\lambda}_{\mathrm{e},q}$) interfaces ($q = 1, 2, 3$). $\hat{c}_q^{\mathrm{bas}}$: molecular basal production; $\hat{\lambda}_{\mathrm{i/e},q}^{\mathrm{ph}}$: physiological permeability.

	S0	S1	S2	S3
$\hat{c}_2$	$\hat{c}_2^{\mathrm{bas}}$	$\hat{c}_2^{\mathrm{bas}}$	$\hat{c}_2^{\mathrm{bas}}$	$1.75\hat{c}_2^{\mathrm{bas}}$
$\hat{c}_3$	$\hat{c}_3^{\mathrm{bas}}$	$2\hat{c}_3^{\mathrm{bas}}$	$2\hat{c}_3^{\mathrm{bas}}$	$2\hat{c}_3^{\mathrm{bas}}$
$\hat{\lambda}_{\mathrm{i},q}$	$\hat{\lambda}_{\mathrm{i},q}^{\mathrm{ph}}$	$\hat{\lambda}_{\mathrm{i},q}^{\mathrm{ph}}$	$0.01\hat{\lambda}_{\mathrm{i},q}^{\mathrm{ph}}$	$0.01\hat{\lambda}_{\mathrm{i},q}^{\mathrm{ph}}$
$\hat{\lambda}_{\mathrm{e},q}$	$\hat{\lambda}_{\mathrm{e},q}^{\mathrm{ph}}$	$\hat{\lambda}_{\mathrm{e},q}^{\mathrm{ph}}$	$\hat{\lambda}_{\mathrm{e},q}^{\mathrm{ph}}$	$\hat{\lambda}_{\mathrm{e},q}^{\mathrm{ph}}$

Since remodelling laws induce variations of μ_{F}, the standard deviation of v_{c}, being equal to $(\hat{\beta}_{\mathrm{F}}^2 + \mu_{\mathrm{F}}^2)^{1/2}$ in the addressed limiting behaviour, is affected by remodelling [74]. For a given function $\mu_{\mathrm{F}}(r, t)$ obtained from equation (5.6), the along-the-thickness mean number n_β of collagen fibres inclined by β_{o}, i.e. $n_\beta = n_\beta(\beta_{\mathrm{o}})$, results from (time dependency omitted)

$$n_\beta(\beta_{\mathrm{o}}) = \frac{N_{\mathrm{F}}}{\delta_{\mathrm{o}}} \int_{r_{\mathrm{i,o}}}^{r_{\mathrm{e,o}}} v_{\mathrm{c}}(\beta_{\mathrm{o}}, \hat{\beta}_{\mathrm{F}}, \mu_{\mathrm{F}}(r))\, \mathrm{d}r, \tag{5.22}$$

where N_{F} is the total number of collagen fibres in the arterial thickness. The number of collagen fibres along different directions can be experimentally measured from polarizing microscope images and image processing techniques [54], obtaining $n_\beta^{\mathrm{exp}} = n_\beta^{\mathrm{exp}}(\beta_{\mathrm{o}})$. Therefore, N_{F} can be estimated as $N_{\mathrm{F}} = \int_{-\pi/2}^{\pi/2} n_\beta^{\mathrm{exp}}(\beta_{\mathrm{o}})\, \mathrm{d}\beta_{\mathrm{o}}$. In particular, addressing human thoracic aortic segments, data in [54] give $N_{\mathrm{F}} = 826$ (function n_β^{exp} reported in [54] has been normalized by the number of subjects considered in the study).

Through-the-thickness integrations in equations (5.12) and (5.22) are performed by employing a standard trapezoidal integration rule with N_{ip} integration points. To be consistent with the repetitive microstructure of arterial tissues which are made up by lamellar units with fairly uniform composition (approx. 60 in the media of human aortas [55,56]), $N_{\mathrm{ip}} = 60$ has been chosen, for the case study under investigation, such that each integration point is representative of a media lamellar unit.

Angular integration in equation (5.14) is performed by considering a discrete distribution of n_{F} fibre families, and hence a discrete set of collagen fibres inclined by $\beta_{\mathrm{o}}^{(a)}$ (with $a = 1, \ldots, n_{\mathrm{F}}$), with

$$n_{\mathrm{F}} \text{ even: } \beta_{\mathrm{o}}^{(a)} = \left(a - \frac{1}{2}\right)\frac{\pi}{n_{\mathrm{F}}} - \frac{\pi}{2} \quad \text{and}$$
$$n_{\mathrm{F}} \text{ odd: } \beta_{\mathrm{o}}^{(a)} = \frac{a\pi}{n_{\mathrm{F}}+1} - \frac{\pi}{2}. \tag{5.23}$$

It is worth highlighting that N_{F} in equation (5.22) represents the number of fibres in the tissue, hence not coinciding with the number n_{F} of the discrete fibre families, introduced only for numerical purposes. In considering the discrete set of angles $\beta_{\mathrm{o}}^{(a)}$, the discrete PDF $v_{\mathrm{c}}^{(a)} = v_{\mathrm{c}}(\beta_{\mathrm{o}}^{(a)}, \hat{\beta}_{\mathrm{F}}, \mu_{\mathrm{F}})$ obtained from the continuous circular distribution in equation (5.21) is normalized for ensuring that $\sum_{a=1}^{n_{\mathrm{F}}} v_{\mathrm{c}}^{(a)} = 1$. To have a fine angular discretization, $n_{\mathrm{F}} = 37$ collagen fibre families (approx. one every 5°) are employed in the numerical application.

Despite the low geometrical dimension of the proposed case study, a relatively large number of parameters are involved. The adopted values have been chosen in order to show the soundness of the proposed approach, and not to provide quantitative indications on a specific clinical study. Therefore, model calibration is based on experimental ranges available from the literature, as described next.

Table 2. Values of parameters for arterial geometry, for the remodelling R and for the transport T problems, together with relevant references. See §5.6.1 for details on model calibration.

symbol	value	definition	references
$r_{i,o}$	8.24 mm	reference internal radius	[40]
δ_o	0.9 mm	reference thickness	[40,54]
α	80°	opening angle	[39]
V_S	0.2	volume fraction of SMCs	[55]
$\bar{C}$	5 pg μg^{-1}	reference concentration	[20]
ν	0.1 year	remodelling viscosity	[73]
D	10^{-5} mm^2 s^{-1}	diffusivity constants	[36,75,76]
$\eta_{1\nu}$	10^{-3} s^{-1}	reaction kinetics rate constant	[25,76]
ζ	10^{-5} s^{-1}	natural decay rate constants	[25,76]
$\hat{\lambda}_i^{ph}$	5×10^{-6} mm s^{-1}	intima permeability	[36,77]
$\hat{\lambda}_e^{ph}$	5×10^{-6} mm s^{-1}	adventitia permeability	[36,77]

5.6.1. Model calibration

As reported in table 2, arterial geometry in the reference configuration is defined in agreement with well-established experimental ranges [39,40,54]. Table 2 reports also the volume fraction of SMCs V_S, which is a common parameter for problems R, T and M. The adopted value corresponds to the data obtained in [55] from confocal imaging.

Addressing remodelling laws (see §5.4), threshold concentrations C_{R1} and C_{R2}, governing the remodelling induced by MMPs and TGFs-β, have been chosen on the basis of two available pieces of evidence: the development of aneurysms is associated with the increase of MMPs in arterial tissues from 2 to 10 pg μg^{-1} [20]; the concentration of TGFs-β following drug-induced aneurysm stabilization reaches up to 5 pg μg^{-1} [20]. Therefore, as physiopathological remodelling is induced by comparable concentrations of MMPs and TGFs-β, concentrations C_{R1} and C_{R2} are assumed to coincide, as well as remodelling viscosities ν_j. Therefore, it is chosen

$$C_{R1} = C_{R2} = \bar{C} \quad \text{and} \quad \nu_1 = \nu_2 = \nu_3 = \nu, \tag{5.24}$$

where $\bar{C}$ is a reference concentration value, chosen in agreement with the afore-introduced data (table 2). Moreover, viscosity ν is set such that remodelling (i.e. functions $s_j(\rho, t)$) reaches the steady state within time intervals of approximately $10\nu = 1$ year (table 2), that is within the typical time scale of the growth of aneurysms [73] and in agreement with the evidence that pathological arterial remodelling evolves within approximately one month [78].

Addressing the transport problem (see §5.3), a number of experimental and numerical works have explored the transport within arterial wall of, for example, low-density-lipoproteins (LDL), albumin or specific drugs [36,75–77]. In particular, well-established documented values for the diffusivity D_L and the permeability λ_L of LDL can be found in [36], i.e. $D_L \approx 10^{-13}$ m^2 s^{-1} and $\lambda_L \approx 50 \times 10^{-8}$ cm s^{-1}. Unfortunately, to the best of the authors' knowledge, well-established values of the diffusivity and of the permeability of MMPs, TGFs-β and ILs in arterial tissues are not available. Accordingly, values for D_q^r and $\hat{\lambda}_{i/e,q}^{ph}$ have been set on the basis of data for LDL, taking into account that diffusivity and permeability scale with molecular weight (LDL molecular weight $Mw_L = 3$ MDa [79]). In particular, a linear inverse relationship for this scaling has been employed [80].

Following these considerations and as values of molecular weight of MMPs (≈50 kDa [81]), ILs (≈30 kDa [82]) and TGFs-β (≈25 kDa [83]) are comparable, no distinction has been made among species for diffusivity and permeability, that is:

$$D_1^r = D_2^r = D_3^r = D \quad \text{and} \quad \hat{\lambda}_{i/e,1}^{ph} = \hat{\lambda}_{e,2}^{ph} = \hat{\lambda}_{i,3}^{ph} = \hat{\lambda}_{i/e}, \tag{5.25}$$

with $D = D_L Mw_L/Mw$ and $\hat{\lambda}_{i/e}^{ph} = \lambda_L Mw_L/Mw$, where Mw is a reference molecular weight chosen equal to 30 kDa (table 2). Analogously, the decay rates ζ_q of the different molecular species can be retained comparable (at least of the order of magnitude) because these have been reported to be 4.32 days^{-1} for MMPs, 3.84 days^{-1} for growth factors and 1.19 days^{-1} for ILs [81]. Accordingly, the following simplifying choice has been adopted:

$$\zeta_1 = \zeta_2 = \zeta_3 = \zeta, \tag{5.26}$$

the value employed for ζ corresponding to a half-life of approximately 1 day (table 2). As regards values of reaction kinetics rate constants η_{1v} (governing MMP production in response to IL/TGF-β stimulation), they have been set as corresponding to a time constant of approximately 15 min (table 2). The latter choice refers to the order of magnitude of an acute inflammation [84] and is made to address an acute responsiveness of SMCs. It is worth highlighting that the rate ζ has been chosen such that the corresponding half-life results at the upper bound of the range reported in [81], in order to have a clear distinction between the molecular kinetics associated with the natural decay and the one with cell responsiveness to biochemical alterations.

Stimulative concentrations γ_2 and γ_3 associated with MMP production from ILs and TGFs-β are, in turn, related to tissue remodelling. Therefore, following analogous considerations that led to equation (5.24), no distinction has been made among molecular species and values of γ_2 and γ_3 have been defined in terms of the reference concentration $\bar{C}$. Furthermore, concentration C_{sat}, over which cell production is saturated, has been chosen as 10-fold of a basal production [85]. Hence, it holds (with $\bar{C}$ in table 2):

$$\gamma_2 = \gamma_3 = \bar{C} \quad \text{and} \quad C_{sat} = 10\bar{C}. \tag{5.27}$$

Finally, as simulation conditions, basal productions $\hat{c}_2^{bas}$ and $\hat{c}_3^{bas}$ of TGFs-β and ILs are chosen coinciding with the different species and equal to

$$\hat{c}_2^{bas} = \hat{c}_3^{bas} = \bar{C}, \tag{5.28}$$

such that an increase from the basal production induces the onset of remodelling (because $C_{Rq} = \hat{c}_q^{bas} = \bar{C}$ from equations (5.24) and (5.28)). It is worth highlighting that due to positions in equations (5.24), (5.27) and (5.28), normalized concentrations $c_q/\bar{C}$ result independent from the value of $\bar{C}$ (see equations (5.4)).

Addressing the mechanical problem (see §5.5), tissue constitutive response depends on measurable structural features. In particular, arterial tissue samples show an elastin-to-collagen content ratio of approximately 3:1 and an elastin volume fraction of approximately 30% [55,86]. Furthermore, the dispersion of collagen fibre distribution has been reported in the range 10°–20° [54,87], and the thickness of collagen fibres approximately 1 µm [46,55]. Moreover, high-performance liquid chromatography allows one to measure the mole fraction density of intermolecular cross-links

Table 3. Structural features undergoing remodelling: values $\bar{s}_j$ of parameters defining tissue structure at homeostasis, together with relevant references. As initial conditions (at $t = -T$), $s_j = \bar{s}_j$ with $V_C^0 = V_E^0 = 0$. See §5.6.1 for details on model calibration. SDM, standard deviation measure.

symbol	value	definition	references
$\bar{V}_E$	0.36	elastin volume fraction	[55,86]
$\bar{V}_C$	0.14	collagen volume fraction	[55,86]
$\bar{\mu}_F$	15.36°	SDM of collagen fibre distribution	[54,87]
$\bar{r}_F$	0.5 μm	collagen fibre radius	[46,55]
$\bar{\Lambda}_c$	1 mol mol^{-1}	inter-molecular cross-link density	[53,88]

in load-bearing collagen fibrils, resulting in approximately 890 mmol mol^{-1} [88]. In agreement with these considerations, the reference values $\bar{\mathcal{S}}$ at homeostasis of structural features in set $\mathcal{S}$, i.e. those undergoing remodelling, have been set, as reported in table 3.

Finally, the values of the remaining structural features affecting arterial mechanics (see §5.5 and appendix A) have been chosen in agreement with well-established physiological ranges [39,40,54,55,89,90], and assumed to be constant in space and time (table 4). Comprehensive explanations on the adopted values can be found in previous works by some of the authors [48,49,53]. In particular, stiffness k_M of non-collagenous constituents is tuned in order to fit experimental pressure–radius data [58] at low pressure range, the resulting optimal value agreeing well with the experimental value of elastin stiffness (approx. 1 MPa [90]).

Data accessibility. This article has no additional data.

Authors' contributions. M.M., G.P., G.V. and P.W. designed the study. M.M. conceived the model and conducted the numerical analyses. G.P. and G.V. helped to refine the model and to discuss the findings. P.W. supervised the whole study and contributed to the interpretation of results. M.M and G.V. wrote the manuscript. All authors gave their final approval for publication.

Funding. G.V. acknowledges the Italian Minister of University and Research, MIUR (Program: 'Consolidate the Foundations 2015'; Project: BIOART; Grant number (CUP): E82F16000850005).

Acknowledgments. M.M. acknowledges that this work has been carried out within the framework of the SMART BIOTECS alliance between the Technical University of Braunschweig and the Leibniz University of Hannover. This initiative is financially supported by the Ministry of Economy and Culture (MWK) of Lower Saxony, Germany.

Appendix A. Multiscale mechanics of collagen fibres

The multiscale homogenization approach employed for the modelling of the multiscale mechanics of collagen fibres is briefly reported here (figure 10). Since the inelastic deformation associated with growth and remodelling is here neglected (see §5.2), the following relationships are obtained under the assumption that the elastic stretch λ_F^e corresponds to the total stretch $\lambda_F = [\mathrm{Tr}(\mathbf{C}_C\mathbf{M}_o(\beta_o))]^{1/2}$, namely $\lambda_F^e = \lambda_F$ (see equations (5.17) and (5.18)).

Collagen fibres are a collection of fibrils, the elongation of which, described by stretch λ_f, is affected by inter-molecular sliding and collagen molecular elongation (figure 10). The

Table 4. Values of structural features affecting arterial mechanics and not undergoing remodelling, together with relevant references (V_S in table 2). See §5.6.1 for details on model calibration.

symbol	value	definition	references
k_M	2.2 MPa	stiffness of non-collagenous constituents	[90]
$\pm\hat{\beta}_F$	±25.8°	peak angles of collagen fibre distribution	[54]
$H_{F,o}$	1.36 μm	reference collagen fibre amplitude	[48,55]
$L_{F,o}$	5 μm	reference collagen fibre period	[48,55]
k_c	105 nN μm^{-1}	inter-molecular cross-link stiffness	[53]
$\ell_{m,o}$	279 nm	reference molecular end-to-end length	[48]
ℓ_c	287 nm	molecular contour length	[48]
ℓ_p	14.5 nm	molecular persistance length	[48]
A_m	1.41 nm^2	molecular cross-sectional area	[48]
$\hat{E}_0$	1 GPa	low-strain triple-helix tangent modulus	[48]
$\hat{E}$	80 GPa	high-strain triple-helix tangent modulus	[48]
η_m	22.5	triple-helix uncoiling resistance	[48]
ε_o^h	0.1	triple-helix uncoiling strain	[48]
ϑ	310 K	body absolute temperature	—

elongation of collagen molecules is described by the stretch λ_m. As schematically depicted in figure 10, molecular elongation depends on *in series* entropic and energetic mechanisms, respectively, described by stretches λ_m^s and λ_m^h [42,51,53].

Recalling that λ_F^e represents the elastic stretch along the main direction of a crimped collagen fibre (i.e. the along-the-chord extension), the multiscale relationships $\lambda_f = \lambda_f(\lambda_F^e)$, $\lambda_m = \lambda_m(\lambda_f)$, $\lambda_m^s = \lambda_m^s(\lambda_m)$ and $\lambda_m^h = \lambda_m^h(\lambda_m)$ lead to the implicit dependences $\lambda_m^s = \lambda_m^s(\lambda_F^e)$ and $\lambda_m^h = \lambda_m^h(\lambda_F^e)$.

The tangent modulus of collagen molecules E_m results in [50]

$$E_m(\lambda_m^s, \lambda_m^h) = \frac{E_m^s(\lambda_m^s)E_m^h(\lambda_m^h)}{E_m^s(\lambda_m^s) + E_m^h(\lambda_m^h)}, \tag{A 1a}$$

where molecular collagen moduli related to entropic mechanisms E_m^s and to energetic mechanisms E_m^h are

$$E_m^s(\lambda_m^s) = \frac{k_B\vartheta\ell_{m,o}}{\ell_p\ell_c A_m}\left[\frac{\ell_c^3}{2(\ell_c - \ell_{m,o}\lambda_m^s)^3} + 1\right] \tag{A 1b}$$

and

$$E_m^h(\lambda_m^h) = \frac{\ell_{m,o}}{\ell_c}\left\{\frac{\hat{E}}{1 + \exp\{-\eta_m[\ell_{m,o}(\lambda_m^h - 1)/\ell_c - \varepsilon_o^h]\}} + \hat{E}_o\right\}, \tag{A 1c}$$

with k_B being the Boltzmann constant and ϑ the absolute body temperature. Moreover, addressing collagen triple helices, ℓ_p is the persistence length, ℓ_c the contour length, $\hat{E}_o$ the low-strain tangent modulus, $\hat{E}$ the high-strain tangent modulus, ε_o^h the uncoiling strain and η_m is the uncoiling resistance [51,53]. Function $\ell_F = \ell_F(\lambda_F^e)$ is defined as $\ell_F(\lambda_F^e) = \lambda_F^e L_{F,o}/4$. Moreover, relationships $\lambda_m^s = \lambda_m^s(\lambda_F^e)$, $\lambda_m^h = \lambda_m^h(\lambda_F^e)$ and $H_F = H_F(\lambda_F^e)$ are determined from the following set of differential equations [50]:

$$\frac{d\lambda_m^s}{d\lambda_F^e} = \Phi_{ms}(\lambda_m^s, \lambda_m^h)\Phi_{fm}(\lambda_m^s, \lambda_m^h)\Phi_f(\lambda_F^e, H_F), \tag{A 2a}$$

$$\frac{d\lambda_m^h}{d\lambda_F^e} = \Phi_{mh}(\lambda_m^s, \lambda_m^h)\Phi_{fm}(\lambda_m^s, \lambda_m^h)\Phi_f(\lambda_F^e, H_F) \tag{A 2b}$$

and

$$\frac{dH_F}{d\lambda_F^e} = -\frac{\ell_F H_F[4(\ell_F^2 + H_F^2) - 3r_F^2]}{\lambda_F^e[4H_F^2(\ell_F^2 + H_F^2) + 3\ell_F^2 r_F^2]}, \tag{A 2c}$$

with $\lambda_m^s(1) = \lambda_m^h(1) = 1$ and $H_F(1) = H_{F,o}$ as initial conditions. Accounting for the chain-rule, equations (A 2*a*) and (A 2*b*) are obtained on the basis of the following interscale relationships:

$$\Phi_{ms}(\lambda_m^s, \lambda_m^h) = \frac{d\lambda_m^s}{d\lambda_m} = \frac{E_m(\lambda_m^s, \lambda_m^h)}{E_m^s(\lambda_m^s)}, \tag{A 3a}$$

$$\Phi_{mh}(\lambda_m^s, \lambda_m^h) = \frac{d\lambda_m^h}{d\lambda_m} = \frac{E_m(\lambda_m^s, \lambda_m^h)}{E_m^h(\lambda_m^h)}, \tag{A 3b}$$

$$\Phi_{fm}(\lambda_m^s, \lambda_m^h) = \frac{d\lambda_m}{d\lambda_f} = \frac{1}{E_m(\lambda_m^s, \lambda_m^h)}\left[\frac{1}{E_m(\lambda_m^s, \lambda_m^h)} + \frac{A_m}{\Lambda_c k_c \ell_{m,o}}\right]^{-1} \tag{A 3c}$$

and

$$\Phi_f(\lambda_F^e, H_F) = \frac{d\lambda_f}{d\lambda_F^e} = \frac{\lambda_F^e \ell_{F,o}^2 + H_F \frac{dH_F}{d\lambda_F^e}}{\sqrt{[(\lambda_F^e)^2 \ell_{F,o}^2 + H_F^2](\ell_{F,o}^2 + H_{F,o}^2)}}. \tag{A 3d}$$

Moreover, equation (A 2*c*) is an evolution equation for fibre geometry, obtained from an application of the principle of virtual works.

For further theoretical details on the multiscale homogenization approach and on previous equations, the readers can refer to the formulation presented by some of the authors in [50].

References

1. Kassab GS. 2006 Biomechanics of the cardiovascular system: the aorta as an illustratory example. *J. R. Soc. Interface* **3**, 719–740. (doi:10.1098/rsif.2006.0138)
2. Fuster V, Kelly B. 2010 *Promoting cardiovascular health in the developing world: a critical challenge to achieve global health*. Washington, DC: National Academy Press.
3. Taylor CA, Humphrey JD. 2009 Open problems in computational vascular biomechanics: hemodynamics and arterial wall mechanics. *Comput. Methods Appl. Mech. Eng.* **198**, 3514–3523. (doi:10.1016/j.cma.2009.02.004)
4. Sagi I, Gaffney JP (eds). 2015 *Matrix metalloproteinase biology*. Hoboken, NJ: Wiley.
5. Lilly B. 2014 We have contact: endothelial cell-smooth muscle cell interactions. *Physiology* **29**, 234–241. (doi:10.1152/physiol.00047.2013)
6. Palombo F, Winlove CP, Edginton RS, Green E, Stone N, Caponi S, Madami M, Fioretto D. 2014 Biomechanics of fibrous proteins of the extracellular matrix studied by Brillouin scattering. *J. R. Soc. Interface* **11**, 20140739. (doi:10.1098/rsif.2014.0739)
7. Ethier CR, Simmons CA. 2007 *Introductory biomechanics—from cells to organisms*. Cambridge, UK: Cambridge University Press.
8. Deguchi JO, Aikawa E, Libby P, Vachon JR, Inada M, Krane SM, Whittaker P, Aikawa M. 2005 Matrix metalloproteinase-13/collagenase-3 deletion promotes collagen accumulation and organization in mouse atherosclerotic plaques. *Circulation* **112**, 2708–2715. (doi:10.1161/CIRCULATIONAHA.105.562041)
9. García-Alvarez J, Ramirez R, Checa M, Nuttall RK, Sampieri CL, Edwards DR, Selman M, Pardo A. 2006 Tissue inhibitor of metalloproteinase-3 is up-regulated by transforming growth factor-β1 in vitro and expressed in fibroblastic foci in vivo in idiopathic pulmonary fibrosis. *Exp. Lung Res.* **32**, 201–214. (doi:10.1080/01902140600817481)
10. Jones JA, Spinale FG, Ikonomidis JS. 2008 Transforming growth factor-β signaling in thoracic aortic aneurysm development: a paradox in pathogenesis. *J. Vasc. Res.* **46**, 119–137. (doi:10.1159/000151766)
11. Kucich U, Rosenbloom JC, Abrams WR, Rosenbloom J. 2002 Transforming growth factor-β stabilizes elastin mRNA by a pathway requiring active Smads, protein kinase C-δ, and p38. *Am. J. Respir. Cell Mol. Biol.* **26**, 183–188. (doi:10.1165/ajrcmb.26.2.4666)
12. Rastogi A, Kim H, Twomey JD, Hsieh AH. 2013 MMP-2 mediates local degradation and remodeling of collagen by annulus fibrosus cells of the intervertebral disc. *Arthritis Res. Ther.* **15**, R57. (doi:10.1186/ar4224)
13. VanderSlot AJ, VanDura EA, DeWit EC, Degroot J, Huizinga TWJ, Bank RA, Zuurmoond AM. 2005 Elevated formation of pyridinoline cross-links by profibrotic cytokines is associated with enhanced lysyl hydroxylase 2b levels. *BBA Mol. Basis Dis.* **1741**, 95–102. (doi:10.1016/j.bbadis.2004.09.009)
14. Visse R, Nagase H. 2003 Matrix metalloproteinases and tissue inhibitors of metalloproteinases structure, function, and biochemistry. *Circ. Res.* **92**, 827–839. (doi:10.1161/01.RES.0000070112.80711.3D)
15. Freedman BR, Bade ND, Riggin CN, Zhang S, Haines PG, Ong KL, Janmey PA. 2015 The (dys) functional extracellular matrix. *BBA Mol. Basis Dis.* **1853**, 3153–3164. (doi:10.1016/j.bbamcr.2015.04.015)
16. Boyle CJ, Lennon AB, Early M, Kelly DJ, Lally C, Prendergast PJ. 2010 Computational simulation methodologies for mechanobiological modelling: a cell-centred approach to neointima development in stents. *Phil. Trans. R. Soc. A* **368**, 2919–2935. (doi:10.1098/rsta.2010.0071)
17. Boyle CJ, Lennon AB, Prendergast PJ. 2013 Application of a mechanobiological simulation technique to stents used clinically. *J. Biomech.* **46**, 918–924. (doi:10.1016/j.jbiomech.2012.12.014)
18. Galis ZS, Khatri JJ. 2002 Matrix metalloproteinases in vascular remodeling and atherogenesis: the good, the bad, and the ugly. *Circ. Res.* **90**, 251–262.
19. Tang PCY, Coady MA, Lovoulos C, Dardik A, Aslan M, Elefteriades JA, Tellides G. 2005 Hyperplastic cellular remodeling of the media in ascending thoracic aortic aneurysms. *Circulation* **112**, 1098–1105. (doi:10.1161/CIRCULATIONAHA.104.511717)
20. Dai J, Michineau S, Franck G, Desgranges P, Becquemin JP, Gervais M, Allaire E. 2011 Long term stabilization of expanding aortic aneurysms by a short course of cyclosporine a through transforming growth factor-beta induction. *PLoS ONE* **6**, e28903. (doi:10.1371/journal.pone.0028903)
21. Marino M, Pontrelli G, Vairo G, Wriggers P 2017 Coupling microscale transport and tissue mechanics: modelling strategies for arterial multiphysics. In *Microscale transport modelling in biological processes* (ed. S Becker), pp. 77–112. Amsterdam, The Netherlands: Elsevier.
22. Braeu FA, Seitz A, Aydin RC, Cyron CJ. 2017 Homogenized constrained mixture models for anisotropic volumetric growth and remodeling. *Biomech. Model. Mechanobiol.* **16**, 889–906. (doi:10.1007/s10237-016-0859-1)
23. Cyron CJ, Aydin RC, Humphrey JD. 2016 A homogenized constrained mixture (and mechanical analog) model for growth and

remodeling of soft tissue. *Biomech. Model. Mechanobiol.* **15**, 1389–1403. (doi:10.1007/s10237-016-0770-9)

24. Comellas E, Gasser TC, Bellomo FJ, Oller S. 2016 A homeostatic-driven turnover remodelling constitutive model for healing in soft tissues. *J. R. Soc. Interface* **13**, 20151081. (doi:10.1098/rsif.2015.1081)
25. Aparício P, Thompson MS, Watton PN. 2016 A novel chemo-mechano-biological model of arterial tissue growth and remodelling. *J. Biomech.* **49**, 2321–2330. (doi:10.1016/j.jbiomech.2016.04.037)
26. Figueroa CA, Baek S, Taylor CA, Humphrey JD. 2009 A computational framework for coupled fluid-solid growth modeling in cardiovascular simulations. *Comput. Methods Appl. Mech. Eng.* **198**, 3583–3602. (doi:10.1016/j.cma.2008.09.013)
27. Humphrey JD. 2009 Vascular mechanics, mechanobiology, and remodeling. *J. Mech. Med. Biol.* **9**, 243–257. (doi:10.1142/S021951940900295X)
28. Watton PN, Ventikos Y, Holzapfel GA. 2009 Modelling the growth and stabilization of cerebral aneurysms. *Math. Med. Biol.* **26**, 133–164. (doi:10.1093/imammb/dqp001)
29. Volokh KY, Vorp DA. 2008 A model of growth and rupture of abdominal aortic aneurysm. *J. Biomech.* **41**, 1015–1021. (doi:10.1016/j.jbiomech.2007.12.014)
30. Baek S, Rajagopal KR, Humphrey JD. 2006 A theoretical model of enlarging intracranial fusiform aneurysms. *J. Biomech. Eng.* **128**, 142–149. (doi:10.1115/1.2132374)
31. Humphrey JD, Rajagopal KR. 2002 A constrained mixture model for growth and remodeling of soft tissues. *Math. Models Methods Appl. Sci.* **12**, 407–430. (doi:10.1142/S0218202502001714)
32. Chooi KY, Comerford A, Sherwin SJ, Weinberg PD. 2016 Intimal and medial contributions to the hydraulic resistance of the arterial wall at different pressures: a combined computational and experimental study. *J. R. Soc. Interface* **13**, 20160234. (doi:10.1098/rsif.2016.0234)
33. D'Errico M, Sammarco P, Vairo G. 2015 Analytical modeling of drug dynamics induced by eluting stents in the coronary multi-layered curved domain. *Math. Biosci.* **267**, 79–96. (doi:10.1016/j.mbs.2015.06.016)
34. Pontrelli G, DeMonte F. 2007 Mass diffusion through two-layer porous media: an application to the drug-eluting stent. *Int. J. Heat Mass Transfer* **50**, 3658–3669. (doi:10.1016/j.ijheatmasstransfer.2006.11.003)
35. S Kenjeres, deLoor A. 2014 Modelling and simulation of low-density lipoprotein transport through multi-layered wall of an anatomically realistic carotid artery bifurcation. *J. R. Soc. Interface* **11**, 20130941. (doi:10.1098/rsif.2013.0941)
36. Dabagh M, Jalali P, Tarbell JM. 2009 The transport of LDL across the deformable arterial wall: the effect of endothelial cell turnover and intimal deformation under hypertension. *Am. J. Physiol. Heart Circ. Physiol.* **297**, H983–H996. (doi:10.1152/ajpheart.00324.2009)
37. Leemasawatdigul K, Gappa-Fahlenkamp H. 2012 Development of a mathematical model to describe the transport of monocyte chemoattractant protein-1 through a three-dimensional collagen matrix. *Cardiovas. Pathol.* **21**, 219–228. (doi:10.1016/j.carpath.2011.09.002)
38. Witthoft A, Yazdani A, Peng Z, Bellini C, Humphrey JD, Karniadakis GE. 2016 A discrete mesoscopic particle model of the mechanics of a multi-constituent arterial wall. *J. R. Soc. Interface* **13**, 20150964. (doi:10.1098/rsif.2015.0964)
39. Auricchio F, Conti M, Ferrara A. 2014 How constitutive model complexity can affect the capability to fit experimental data: a focus on human carotid arteries and extension/inflation data. *Arch. Comput. Methods E* **21**, 273–292. (doi:10.1007/s11831-014-9105-0)
40. Holzapfel GA, Ogden RW. 2010 Modelling the layer-specific three-dimensional residual stresses in arteries, with an application to the human aorta. *J. R. Soc. Interface* **7**, 787–799. (doi:10.1098/rsif.2009.0357)
41. Holzapfel GA, Gasser TC, Ogden RW. 2000 A new constitutive framework for arterial wall mechanics and a comparative study of material models. *J. Elasticity* **61**, 1–48. (doi:10.1023/A:1010835316564)
42. Fratzl P. 2008 *Collagen: structure and mechanics*. New York, NY: Springer.
43. Carmo M, Colombo L, Bruno A, Corsi FRM, Roncoroni L, Cuttin MS, Radice F, Mussini E, Settembrini PG. 2002 Alteration of elastin, collagen and their cross-links in abdominal aortic aneurysms. *Eur. J. Vasc. Endovasc. Surg.* **23**, 543–549. (doi:10.1053/ejvs.2002.1620)
44. Brüel A, Ørtoft G, Oxlund H. 1998 Inhibition of cross-links in collagen is associated with reduced stiffness of the aorta in young rats. *Atherosclerosis* **140**, 135–145. (doi:10.1016/S0021-9150(98)00130-0)
45. Tsamis A, Krawiec JT, Vorp DA. 2013 Elastin and collagen fibre microstructure of the human aorta in ageing and disease: a review. *J. R. Soc. Interface* **10**, 20121004. (doi:10.1098/rsif.2012.1004)
46. Robertson AM, Duan X, Aziz KM, Hill MR, Watkins SC, Cebral JR. 2015 Diversity in the strength and structure of unruptured cerebral aneurysms. *Ann. Biomed. Eng.* **43**, 1502–1515. (doi:10.1007/s10439-015-1252-4)
47. Maceri F, Marino M, Vairo G. 2013 Age-dependent arterial mechanics via a multiscale elastic approach. *Int. J. Comput. Methods Eng. Sci. Mech.* **14**, 141–151. (doi:10.1080/15502287.2012.744114)
48. Marino M, Vairo G. 2013 Multiscale elastic models of collagen bio-structures: from cross-linked molecules to soft tissues. In *Multiscale computer modeling in biomechanics and biomedical engineering* (ed. A Gefen), pp. 73–102. Berlin, Germany: Springer.
49. Marino M, Vairo G. 2014 Computational modelling of soft tissues and ligaments. In *Computational modelling of biomechanics and biotribology in the musculoskeletal system* (ed. Z Jin), pp. 141–172. Cambridge, UK: Woodhead Publishing.
50. Marino M, Wriggers P. 2017 Finite strain response of crimped fibers under uniaxial traction: an analytical approach applied to collagen. *J. Mech. Phys. Solids* **98**, 429–453. (doi:10.1016/j.jmps.2016.05.010)
51. Maceri F, Marino M, Vairo G. 2012 Elasto-damage modeling of biopolymer molecules response. *Comput. Model. Eng. Sci.* **87**, 461–481. (doi:10.3970/cmes.2012.087.461)
52. Marino M, Vairo G. 2014 Influence of inter-molecular interactions on the elasto-damage mechanics of collagen fibrils: a bottom-up approach towards macroscopic tissue modeling. *J. Mech. Phys. Solids* **73**, 38–54. (doi:10.1016/j.jmps.2014.08.009)
53. Marino M. 2016 Molecular and intermolecular effects in collagen fibril mechanics: a multiscale analytical model compared with atomistic and experimental studies. *Biomech. Model. Mechanobiol.* **15**, 133–154. (doi:10.1007/s10237-015-0707-8)
54. Schriefl AJ, Zeindlinger G, Pierce DM, Regitnig P, Holzapfel GA. 2011 Determination of the layer-specific distributed collagen fibre orientations in human thoracic and abdominal aortas and common iliac arteries. *J. R. Soc. Interface* **9**, 1275–1286. (doi:10.1098/rsif.2011.0727)
55. O'Connell MK *et al*. 2008 The three-dimensional micro- and nanostructure of the aortic medial lamellar unit measured using 3D confocal and electron microscopy imaging. *Matrix Biol.* **27**, 171–181. (doi:10.1016/j.matbio.2007.10.008)
56. Wolinsky H, Glagov S. 1967 A lamellar unit of aortic medial structure and function in mammals. *Circ. Res.* **20**, 99–111. (doi:10.1161/01.RES.20.1.99)
57. Chen H, Liu Y, Slipchenko MN, Zhao X, Cheng JX, Kassab GS. 2011 The layered structure of coronary adventitia under mechanical load. *Biophys. J.* **101**, 2555–2562. (doi:10.1016/j.bpj.2011.10.043)
58. Hallock P, Benson IC. 1937 Studies on the elastic properties of human isolated aorta. *J. Clin. Invest.* **16**, 595–602. (doi:10.1172/JCI100886)
59. Michel JB, Thaunat O, Houard X, Meilhac O, Caligiuri G, Nicoletti A. 2007 Topological determinants and consequences of adventitial responses to arterial wall injury. *Arterioscler. Thromb. Vasc. Biol.* **27**, 1259–1268. (doi:10.1161/ATVBAHA.106.137851)
60. Lee E, Grodzinky AJ, Libby P, Clinton SK, Lark MW, Lee RT. 1995 Human vascular smooth muscle cell-monocyte interactions and metalloproteinase secretion in culture. *Arterioscler. Thromb. Vasc. Biol.* **15**, 2284–2289. (doi:10.1161/01.ATV.15.12.2284)
61. Maiellaro K, Taylor WR. 2007 The role of the adventitia in vascular inflammation. *Cardiovasc. Res.* **75**, 640–648. (doi:10.1016/j.cardiores.2007.06.023)
62. Bianchi D, Monaldo E, Gizzi A, Marino M, Filippi S, Vairo G. 2017 A FSI computational framework for vascular physiopathology: a novel flow-tissue multiscale strategy. *Med. Eng. Phys.* **47**, 25–37. (doi:10.1016/j.medengphy.2017.06.028)

63. Stenmark KR, Mecham RP. 1997 Cellular and molecular mechanisms of pulmonary vascular remodeling. *Annu. Rev. Physiol.* **59**, 89–144. (doi:10.1146/annurev.physiol.59.1.89)
64. Bianchi D, Marino M, Vairo G. 2016 An integrated computational approach for aortic mechanics including geometric, histological and chemico-physical data. *J. Biomech.* **49**, 2331–2340. (doi:10.1016/j.jbiomech.2016.01.045)
65. Holzapfel GA, Niestrawska JA, Ogden RW, Reinisch AJ, Schriefl AJ. 2015 Modelling non-symmetric collagen fibre dispersion in arterial walls. *J. R. Soc. Interface* **12**, 20150188. (doi:10.1098/rsif.2015.0188)
66. Niestrawska JA, Viertler C, Regitnig P, Cohnert TU, Sommer G, Holzapfel GA. 2016 Microstructure and mechanics of healthy and aneurysmatic abdominal aortas: experimental analysis and modelling. *J. R. Soc. Interface* **13**, 20160620. (doi:10.1098/rsif.2016.0620)
67. Bothe D, Dreyer W. 2015 Continuum thermodynamics of chemically reacting fluid mixtures. *Acta Mech.* **226**, 1757–1805. (doi:10.1007/s00707-014-1275-1)
68. Menzel A, Kuhl E. 2012 Frontiers in growth and remodeling. *Mech. Res. Commun.* **42**, 1–14. (doi:10.1016/j.mechrescom.2012.02.007)
69. Ambrosi D, Guillou A. 2007 Growth and dissipation in biological tissues. *Contin. Mech. Thermodyn.* **19**, 245–251. (doi:10.1007/s00161-007-0052-y)
70. Taber LA. 1995 Biomechanics of growth, remodeling, and morphogenesis. *Appl. Mech. Rev.* **48**, 487–545. (doi:10.1115/1.3005109)
71. Vandermeer J. 2010 How populations grow: the exponential and logistic equations. *Nat. Educ. Knowl.* **3**, 15.
72. Harjanto D, Zaman MH. 2013 Modeling extracellular matrix reorganization in 3D environments. *PLoS ONE* **8**, e52509. (doi:10.1371/journal.pone.0052509)
73. Vardulaki KA, Prevost TC, Walker NM, Day NE, Wilmink ABM, Quick CRG, Ashton HA, Scott RAP. 1998 Growth rates and risk of rupture of abdominal aortic aneurysms. *Br. J. Surg.* **85**, 1674–1680. (doi:10.1046/j.1365-2168.1998.00946.x)
74. Frühwirth-Schnatter S. 2016 *Finite mixture and Markov switching models*. New York, NY: Springer.
75. Thiriet M. 2008 *Biology and mechanics of blood flows—Part II: mechanics and medical aspects*. Berlin, Germany: Springer.
76. Cilla M, Peña E, Martinez MA. 2013 Mathematical modelling of atheroma plaque formation and development in coronary arteries. *J. R. Soc. Interface* **11**, 20130866. (doi:10.1098/rsif.2013.0866)
77. Tarbell JM. 2003 Mass transport in arteries and the location of atherosclerosis. *Annu. Rev. Biomed. Eng.* **5**, 79–118. (doi:10.1146/annurev.bioeng.5.040202.121529)
78. Pasterkampa G, de Kleijna DPV, Borst C. 2000 Arterial remodeling in atherosclerosis, restenosis and after alteration of blood flow: potential mechanisms and clinical implications. *Cardiovasc. Res.* **45**, 843–852. (doi:10.1016/S0008-6363(99)00377-6)
79. Kahlon TS, Shore VG, Lindgren FT. 1992 Heterogeneity of molecular weight and apolipoproteins in low density lipoproteins of healthy human males. *Lipids* **27**, 1055–1057. (doi:10.1007/BF02535588)
80. Valencia DP, González FJ. 2011 Understanding the linear correlation between diffusion coefficient and molecular weight. A model to estimate diffusion coefficients in acetonitrile solutions. *Electrochem. Commun.* **13**, 129–132. (doi:10.1016/j.elecom.2010.11.032)
81. Hao W, Friedman A. 2014 The LDL-HDL profile determines the risk of atherosclerosis: a mathematical model. *PLoS ONE* **9**, e90497. (doi:10.1371/journal.pone.0090497)
82. Mizel SB. 1989 The interleukins. *FASEB J.* **3**, 2379–2388.
83. Gao CF, Kong XT, Gressner AM, Weiskirchen R. 2001 The expression and antigenicity identification of recombinant rat TGF-bold italic beta1 in bacteria. *Cell Res.* **11**, 95–100. (doi:10.1038/sj.cr.7290073)
84. Allison F, Smith MR, Wood WB. 1955 Studies on the pathogenesis of acute inflammation. *J. Exp. Med.* **102**, 655–668. (doi:10.1084/jem.102.6.655)
85. Kehrl JH, Wakefield LM, Roberts AB, Jakowlew S, Alvarez-Mon M, Derynck R, Sporn MB, Fauci AS. 1986 Production of transforming growth factor beta by human T lymphocytes and its potential role in the regulation of T cell growth. *J Exp. Med.* **163**, 1037–1050. (doi:10.1084/jem.163.5.1037)
86. Glagov S, Grande J, Vesselinovitch D, Zarins CK. 1981 Quantification of cells and fibers in histological sections of arterial walls: advantages of contour tracing on a digitizing plate. In *Connective tissues in arterial and pulmonary disease* (eds TF McDonald, AB Chandler), pp. 57–93. New York, NY: Springer.
87. Sugita S, Matsumoto T. 2017 Multiphoton microscopy observations of 3D elastin and collagen fiber microstructure changes during pressurization in aortic media. *Biomech. Model. Mechanobiol.* **16**, 763–773. (doi:10.1007/s10237-016-0851-9)
88. Svensson RB, Mulder H, Kovanen V, Magnusson SP. 2013 Fracture mechanics of collagen fibrils: influence of natural cross-links. *Biophys J.* **104**, 2476–2484. (doi:10.1016/j.bpj.2013.04.033)
89. Åstrand H, Stålhand J, Karlsson M, Sonesson B, Länne T. 2001 In vivo estimation of the contribution of elastin and collagen to the mechanical properties in the human abdominal aorta: effects of age and sex. *J. Appl. Phys.* **110**, 176–187. (doi:10.1152/japplphysiol.00579.2010)
90. Guthold M, Liu W, Sparks EA, Jawerth LM, Peng L, Falvo M, Superfine R, Hantgan RR, Lord ST. 2007 A comparison of the mechanical and structural properties of fibrin fibers with other protein fibers. *Cell Biochem. Biophys.* **49**, 165–181. (doi:10.1007/s12013-007-9001-4)